Dynamics of the Asian Summer Monsoon Anticyclone: Insights from Potential Vorticity Tendency Diagnostics

Ninghui Li[1], Jonathon S. Wright[1], Philip Rupp[2], Alison Ming[3], Shenglong Zhang[1], and Jie Gao[4]

[1]Department of Earth System Science, Ministry of Education Key Laboratory for Earth System Modeling, Tsinghua University, Beijing 100084, China

[2]Meteorological Institute Munich, Ludwig-Maximilian University Munich, Munich 80333, Germany

[3]Department of Applied Mathematics and Theoretical Physics, University of Cambridge, Cambridge CB3 0WA, United Kingdom

[4]Laoshan Laboratory, Qingdao 266237, China

Correspondence: Jie Gao (jgaots2017@163.com) and Jonathon Wright (jswright@tsinghua.edu.cn)

Abstract. The Asian Summer Monsoon Anticyclone (ASMA)is a , the dominant circulation in the upper troposphere and lower stratosphere (UTLS) during boreal summer and exhibits pronounced temporal and spatial the boreal summer, undergoes pronounced spatio-temporal variability. While its time-mean structure and climatological characteristics are the climatological mean state of the ASMA is well documented, the mechanisms governing its temporal evolution, particularly its eastward and westward longitudinal propagation, episodic eddy-shedding eddy shedding events, and the emergence of multimodal behavior are remaining multimodal transient behavior remain incompletely understood. Using multiple reanalysis datasets (In this study, we investigate the dynamic behavior of the ASMA using the reanalysis products JRA-3Q, ERA5, , and MERRA-2) from 2000–2020, this studyanalyzes the dynamic structures of the ASMA, the analysis shows that the ASMA exhibits a trimodalstructure with centers during 2000–2020. The ASMA is primarily trimodal, with core centers situated over the Iranian Plateau, the Tibetan Plateau, and western Pacific , identified via the Western Pacific in all three reanalyses. To differentiate between persistent and transient anticyclonic features, we apply a multi-center vortex tracking algorithm applied to to Montgomery stream function on the 370 K isentropic surfaceto distinguish persistent and transient anticyclones. Further results show that mean zonal and meridional advection are the primary drivers of . Although potential vorticity (PV) tendency, while tendencies are dominated by mean zonal and meridional advection, total diabatic heating that plays a crucial plays a critical modulating role in ASMA evolution . A key contribution of this work lies in the formulation and application of the evolution of anticyclonic vortices within the ASMA. For further insight, we develop and apply an ASMA-specific PV tendency diagnostic , which builds upon established PV budget and enables a more rigorous quantification of the respective roles of dynamical and thermodynamical processes in the anticyclone's intensification and zonal propagation across its three modes. This diagnostic decomposes that decomposes the total PV tendency into dynamic components (e.g., dynamical (horizontal and vertical advection) and thermodynamic components (e.g., (latent heating and background radiation) , enabling the separation of the combined effects of anticyclone propagation and intensification by capturing components. The diagnostic highlights a characteristic tripole pattern of PV tendency . Compared to conventional methods, this new diagnostic provides a more rigorous and precise quantification of the physical processes governing the ASMA's zonal movements and overall development, thereby

advancing our scientific understanding of the ASMA's variability and underlying mechanisms in the UTLS regionwithin vortices, separating propagation effects from intensification and thereby providing a clearer physical attribution of the zonal movement of vortices within the ASMA.

1 Introduction

The Asian summer monsoon anticyclone Summer Monsoon Anticyclone (ASMA) is a prominent atmospheric circulation feature during boreal summer, manifesting as an extensive anticyclonic vortex in defining feature of the upper troposphere and lower stratosphere (UTLS) during the boreal summer. Bounded by the subtropical westerly jet to the north and the tropical easterly jet to the south, the ASMA resides at the interface straddles the boundary between the tropics and subtropics and extends vertically from approximately between ∼300to hPa and 70hPa hPa (Hsu et al., 1999; Randel and Park, 2006; Nützel et al., 2016; Manney et al., 2021). The ASMA is fundamentally driven driven primarily by diabatic heating associated with the Asian summer monsoon. Strong land–sea thermal contrasts Summer Monsoon (Hoskins and Rodwell, 1995). Strong land–sea thermal contrasts and abundant moisture south of the Himalayas induce low-level convergence over the Asian continent and adjacent oceans, promoting deep ascent and convection over elevated terrain such as the Iranian and Tibetan plateaus . The associated convective diabatic heating amplifies South Asia, promoting ascent and deep convection, particularly along the southern slope of the Tibetan Plateau (Fu et al., 2006; Qie et al., 2014). The strong diabatic heating associated with this convection imposes upper-tropospheric divergence, which in turn leads to causing the formation and maintenance of a the large-scale anticyclonic circulation in the UTLS. The UTLS region influenced by the ASMA is also characterized by the presence of the Asian tropopause aerosol layer, which can at upper levels (Garny and Randel, 2013; Siu and Bowman, 2020). At the peak of the monsoon, warm anomalies in the monsoon upper troposphere are large enough to cause a regional reversal of the meridional temperature gradient between the equator and the core of the anticyclone, yielding a broad region of angular momentum-conserving flow defined by small values of potential vorticity. Water vapor and pollutants accumulate within the boundaries of this flow and interact with the anticyclonic circulation and circulation to modulate its structure and variability (Vernier et al., 2015; Santee et al., 2017; Bian et al., 2020; Honomichl and Pan, 2020). Despite this well-established conceptual framework, the ASMA exhibits pronounced mechanisms governing the intraseasonal and interannual variability linked to variations in surface of the ASMA, which emerge from fluctuations in heating and subtropical jet dynamics , and the mechanisms governing this variability remain an active area of research among other processes, remain a subject of active scientific inquiry (Garny and Randel, 2013; Ren et al., 2019; Manney et al., 2021; Rupp and Haynes, 2021).

A variety of Various diagnostic approaches have been used developed to characterize the spatial extent, location, modality and other structural aspects and modality of the ASMA, reflecting . The breadth of these approaches reflects both the dynamical complexity of the system and the availabilityASMA and its importance, as well as changes in data availability, such as the development of long-term reanalysis datasets. Observational analyses have shown products. Observational studies demonstrate that the ASMA exhibits pronounced significant temporal variability, including large-amplitude east–west east–west oscillations and systematic center vortex propagation on intraseasonal timescales (Zhang et al., 2002; Nützel et al., 2016). Rather than ~~remaining~~ a single, broad, coherent vortex, the ~~anticyclonic~~ circulation frequently reorganizes, with ~~circulation centers alternately intensifying over~~ centers of intensity alternating between the Iranian Plateau (IP), the Tibetan Plateau (TP), and the ~~western~~ Western Pacific. These zonal ~~movements~~ shifts are often accompanied by structural ~~instabilities, including vortex splitting , merging, and episodic eddy-shedding events . Previous studies have employed a range of diagnostics. The horizontal extent, location, and modality of the ASMA have commonly been identified using~~ instability, resulting in vortex splitting and merging, as well as episodic eddy shedding events wherein subsidiary anticyclonic vortices break off from the primary circulation (Popovic and Plumb, 2001; Yan et al., 2018; Siu and Bowman, 2020). Previous research has employed a wide range of metrics to track these movements and describe the time-mean circulation in which they are embedded. Common metrics include geopotential height and zonal wind fields at the 100~~and~~ hPa or 200~~hPa~~ hPa levels (Zhang et al., 2002; Qian et al., 2002; Wei et al., 2014; Nützel et al., 2016; Wang et al., 2022), ~~as well as PV~~potential vorticity (PV) on isentropic surfaces between 360 K and 380~~K . Streamfunction-based diagnostics, including the Montgomery streamfunction~~ K (Garny and Randel, 2013; Ploeger et al., 2015; Amemiya and Sato, 2018; Rupp and Haynes, 2020), and Montgomery stream function (MSF) on isentropic surfaces~~, have also been widely used to track the evolution of the ASMA and its eddy-shedding behavior that the westward and eastward anticyclones breaking off form the main anticyclone . In addition, numerical model~~ (Santee et al., 2017; Manney et al., 2021). Numerical simulations and idealized experiments have ~~provided valuable~~ also provided considerable insight into the roles of both ~~natural~~ internal variability and anthropogenic forcing in shaping the anticyclonic ~~circulation~~ structure (Popovic and Plumb, 2001; Amemiya, 2018; Amemiya and Sato, 2018; Rupp and Haynes, 2020; Tweedy et al., 2021; Pan et al., 2022). A summary of ~~commonly used diagnostics and definitions of ASMA location~~ common diagnostics is provided in Table ~~1. Despite~~ 1. However, despite these extensive efforts, substantial challenges remain. ~~Diagnosed ASMA characteristics can differ across~~ ASMA characteristics often vary across different reanalysis products, and ~~ongoing updates to data assimilation systems may further amplify such discrepancies~~changes in assimilated observations can exacerbate these discrepancies (Nützel et al., 2016; Manney et al., 2021). ~~The~~ Furthermore, the frequent coexistence of ~~multiple anticyclonic centers and their zonal migration imply~~ two, three, or more concurrent circulation centers suggests that approaches emphasizing a single dominant vortex or a time-mean structure are ~~often insufficient . Observational evidence indicates that the ASMA frequently consists of two or more concurrent circulation centers, and in some cases more than three, highlighting the need for diagnostic that~~ unable to fully describe the dynamic anticyclone (Zhang et al., 2002; Siu and Bowman, 2020; Rupp and Haynes, 2021). This limitation highlights the need for new diagnostic frameworks that can explicitly account for ~~its~~ the multi-center and multimodal ~~structure~~nature of the ASMA.

The development and intensification of the ASMA are ~~commonly examined~~ frequently evaluated using diagnostics that ~~describe~~ characterize the evolution of its ~~low-PV core. A frequently used measure is the time variation of the~~ low-potential vorticity (PV) core (Ploeger et al., 2015). One common metric is the area enclosed by low-PV contours, as ~~diabatic heating~~ the ascending motion, diabatic heating, and upper-level divergence associated with deep convection ~~act to expand~~ dilute PV and thus expand the area of low-PV regions ~~in the UTLS~~within the UTLS (Garny and Randel, 2013). Complementary diagnostics, such as geopotential height anomalies relative to the zonal mean and ~~variations in streamfunction~~Montgomery stream function, have also ~~been shown to capture~~ proven effective in capturing key aspects of ~~ASMA evolution . Despite their methods~~the

ASMA (Xue et al., 2020; Manney et al., 2021; Zhang et al., 2021). However, these diagnostics ~~have~~ face significant limitations when applied to the ASMA. ~~Low-PV is already present~~ PV is already relatively low over the Asian monsoon region at the ~~onset~~ beginning of boreal summer, and the seasonal evolution of the background ~~PV field is characterized~~ state is marked by a gradual increase in mean PV. ~~This background evolution complicates attempts to disentangle intrinsic~~ This evolving background complicates efforts to disentangle ASMA intensification from ~~changes inherited from preexisting conditions. Moreover, although~~ inherited pre-existing conditions. Furthermore, while PV-area ~~based~~ diagnostics are conceptually ~~motivated by analogous~~ derived from studies of the stratospheric polar vortex, the underlying physical ~~processes differ substantially~~drivers are considerably different. In the polar vortex, diabatic ~~heating~~ cooling and transport barriers ~~play a dominant role, whereas~~ are the primary determinants of structure, while the ASMA is ~~strongly influenced~~ governed by deep convection, divergent outflow, and complex interactions with the subtropical jet~~, limiting~~ . These differences limit the direct transferability of polar vortex diagnostics to the monsoon ~~anticyclone. These challenges highlight the need for diagnostic that can explicitly separate~~ system. Consequently, there is a need for a diagnostic framework that can isolate ASMA intensification from zonal propagation and background PV evolution, while ~~remaining applicable to its~~ providing a robust description of the multi-center ~~and time varying structure~~ dynamic structure of the anticyclone. Addressing this ~~need~~ requirement requires diagnostics that quantify not only the magnitude and distribution of low-PV anomalies but also the ~~processes governing their temporal tendencies~~specific physical processes driving their evolution in time.

In this study, we track ~~ASMA movements and occurrence based on the method by~~ the movement and occurrence of vortex centers within the anticyclone following the methodology of Siu and Bowman (2020), with ~~particular focus on intercomparisons across~~ a specific focus on intercomparison across multiple recent reanalysis products ~~to quantify the anticyclone's~~ and with respect to both persistent and transient ~~behaviors. Additionally, we use~~ vortices. We further introduce a PV tendency diagnostic ~~to quantify ASMA intensification , which provides deeper insights~~ that quantifies ASMA intensification and provides deeper insight into the physical mechanisms governing its ~~westward/eastward~~ zonal propagation and overall ~~development. Section 2 details the datasets , followed by descriptions of~~ structural development. The remainder of this paper is organized as follows. We describe the datasets in Section 2 and the isentropic vortex tracking methodology and the formulation of the PV tendency equation ~~calculations in Section3. Key findings are presented in Section4, and Section5 and 6 include conclusions and discussions of the results~~in Section 3. We then present the findings in Section 4, followed by a discussion in Section 5 and a summary of the key conclusions in Section 6.

2 Data

~~Climate research relies heavily on observational data for validating frameworks, predicting changes, and testing multi-scale process understanding, but these intricate processes often require reanalysis products due to observational limitations .~~ In this study, we analyze variations of the ASMA in three of the most recent ~~'full input' reanalysis products~~'full input' reanalysis products (Fujiwara et al., 2017): the European Centre for Medium-Range Weather Forecasts (ECMWF) Fifth Reanalysis of the Atmosphere (ERA5; Hersbach et al., 2020); the Modern-Era Retrospective Analysis for Research and Applications, Version 2

Table 1. Overview of ~~studies for determining~~ methods used to determine the locations of the ASMA ~~. Geopotential height~~based on geopotential (Φ), zonal wind (u), and relative vorticity ~~are denoted by ϕ, u, and~~ (ζ~~, respectively~~) on pressure surfaces and potential vorticity (PV) and Montgomery stream function (MSF) on isentropic surfaces.

Reference	Dataset	Analysis Period	Variables Analyzed	Identification Method
Zhou et al. (2006)	NCEP-R1	June-August 1950–1999	Φ at 100 hPa	Maximum Φ
Zhang et al. (2002)	NCEP-R1	July-August 1980–1994	Φ, u at 100 hPa	Maximum Φ along ridgeline[a]
Qian et al. (2002)	NCEP-R1	July-August 1958–1997	Φ, u at 100 hPa	Maximum Φ along ridgeline
Yan et al. (2011)	NCEP-R1	June-August 2005–2009	Φ, u at 100 hPa	Maximum Φ along ridgeline
Nützel et al. (2016)	Multiple	June-December 1979–2014	Φ, u at 100 hPa	Maximum Φ along ridgeline
Wei et al. (2014)	ERA-40	June-August 1958–2002	Φ, u at 200 hPa	Maximum Φ along ridgeline
Honomichl and Pan (2020)	ERA-I	July-August 1979–2017	Φ, u at 100 hPa, 150 hPa	Maximum Φ along ridgeline
Zarrin et al. (2010)	NCEP-R1	June-August 1971–2000	Φ, ζ at 100 hPa	Max Φ along ridgeline; max negative ζ
Garny and Randel (2013)	MERRA	May-September 2005–2009	PV at 360/380 K	PV threshold
Fairlie et al. (2014)	GEOS-5.2	June 2011	PV at 380 K	PV threshold
Amemiya and Sato (2018)	ERA-I	June-August 1979–2016	PV at 360/370/380 K	PV threshold
Ploeger et al. (2015)	ERA-I	June-August 1979–2014	PV at 380 K	PV gradient
Popovic and Plumb (2001)	NCEP-R1	July 1987–1990	MSF, PV at 370 K	Maximum MSF; PV threshold
Siu and Bowman (2020)	ERA-I	May-September 1979–2018	MSF, u, ζ at 370 K	MSF local maxima; zero zonal wind $\pm\zeta$
Santee et al. (2017)	GEOS-5.9	June-August 2005-2014	MSF at 350/370/390/410 K	MSF thresholds[b]
Manney et al. (2021)	Multiple	April-October 1958-2018	MSF at 350/370/390/410 K	MSF thresholds[b]
Kachula et al. (2025)	ERA5	April-October 1980-2023	MSF at 350/370/390/410 K	MSF ratio

[a]Ridgeline is defined as the zero contour in zonal wind

[b]MSF threshold values: 350 K: 344800 $m^2 s^{-2}$; 370 K: 356500 $m^2 s^{-2}$; 390 K: 367100 $m^2 s^{-2}$; 410 K: 377300 $m^2 s^{-2}$

(MERRA-2; Gelaro et al., 2017), and the Japanese Reanalysis for Three Quarters of a Century (JRA-3Q; Kosaka et al., 2024). Our study covers the warm seasons of the Northern Hemisphere (May to September) ~~of 2000-2020~~during 2000–2020. All reanalysis products are interpolated to a common $1.25° \times 1.25°$ latitude-longitude grid and ~~subselected~~ subsampled in time to produce ~~6-hour fields. The key~~ 6-hourly fields. Analyses are performed on the 100 hPa isobaric level and the 370 K isentropic surface. Key details of the reanalysis products are listed in Table 2. ~~The~~

In addition to standard products such as temperatures and winds, we use the physical temperature tendencies from each reanalysis. These tendencies include heating due to radiative flux convergence, cloud physics and convection, turbulent mixing, and other parameterized processes affecting temperature, such as gravity wave drag. The decomposition of these terms differs across the reanalyses. For example, ERA5 ~~dataset does not provide a direct product for latent heating. Therefore, this study adopts the combination of top net shortwave radiation~~ provides temperature tendencies due to all parameterized physics (mttpm) along with shortwave (mttswr) ~~, top net longwave radiation~~ and longwave (mttlwr) ~~, and precipitation-related top latent heat flux (mttpm) to indirectly characterize latent heating. Among them, mttswr and mttlwrjointly depict the radiation budget balance at the top of~~ radiative heating. Non-radiative heating, calculated as mttpm − (mttswr + mttlwr), provides a close approximation to deep convective heating in the monsoon UTLS (Tegtmeier et al., 2022), with temperature tendencies due to other non-radiative processes roughly two orders of magnitude smaller than those due to convection in the upper troposphere (Wright and Fueglistaler, 2013). MERRA-2 provides a more complete breakdown, including terms due to radiative heating (DTDTRAD), moist physics (DTDTMST), gravity wave drag (DTDTGWD), turbulent mixing (DTDTTRB), and data assimilation (DTDTANA). For the following analysis, we use DTDTRAD to represent radiative heating and DTDTMST to represent latent heating. For JRA-3Q, radiative heating is calculated as the sum of longwave (ttlwr) and shortwave (ttswr) components, while latent is calculated as the sum of convective heating (cnvhr) and large-scale moist physics (lrghr), leaving out turbulent mixing (vdfhr). We adopt this approach both to provide a more complete accounting of how different physical processes contribute to PV tendencies across these three reanalyses, and to more precisely identify the influences of vertical gradients in diabatic heating on PV. Calculations of apparent heating (often termed Q1) as a residual of the thermodynamic equation are especially uncertain in these regions, where numerical errors and the ~~atmosphere, providing a thermal background field for latent heat release. mttpm directly corresponds to the latent heat released by water vapor phase change during precipitation, which is the core contributor to latent heating~~inability to fully represent resolved transport lead to large errors even in climatological budgets (Martineau et al., 2018; Wright et al., 2025). ~~The combination of these three variables can effectively make up for the lack of direct latent heating products in ERA5 and accurately reflect the spatiotemporal variation characteristics of latent heating.~~

3 Methodology

3.1 Vortex Tracking

The multi-center ~~anticyclone tracking method~~ tracking algorithm employed in this study ~~is proposed by~~ follows the approach of Siu and Bowman (2020)~~which is based on the single center vortices~~ , which builds upon the single-vortex detection method

Table 2. Details of the three reanalysis products used in this work. All products are interpolated to a common 1.25°×1.25° latitude–longitude grid and subsampled to 6-hourly frequency.

Name	**Source**	**Model Horizontal Resolution Grid**	**Pressure Levels Vertical Range (No. Levels)**	**FrequencyAnalysis Freq.**
ERA5	ECMWF	0.75° × 0.75° T_L639 (∼31 km)	1000 to 50 hPa (37Surface to 1 Pa (137)	6h 1 h
MERRA-2	NASA GMAO	0.625° × 0.5°	1000 to 0.1 hPa (42Surface to 1 Pa (72)	6h 3 h
JRA-3Q	JMA	1.25° × 1.25° T_L479 (∼40 km)	1000 to 0.1 hPa (45Surface to 1 Pa (100)	6h 6 h

of Zhang et al. (2002). Three variables from reanalysis data are used to locate the centers of ASMA, including zonal wind , To locate centers of the ASMA, we use three variables taken directly or computed from reanalysis datasets: zonal wind (u, MSF, ψ, and relative vorticity,), Montgomery stream function (MSF $= c_pT + \Phi$, where T is temperature, Φ is geopotential, and c_p is the specific heat at constant pressure), and relative vorticity (ζ.).

The first step is to determine the zonal zero-wind lines for the designated domain (spatial range of 15°–45°N and 0°–180 °E for ASMA) at a specified analysis time (usually 6 hours) as the zero-wind contours involves identifying the zonal-wind ridgeline ($u = 0$) within the designated spatial domain (15°–45°N, 0°–180°E) at each 6-hourly analysis snapshot. This approach is motivated by the observation that the zero-zonal wind contour is nearly zonal inside the AMA within the ASMA (Siu and Bowman, 2020). A Marching Squares Algorithm is employed We apply a marching squares algorithm to identify the isopleths of the zonal wind field $u = 0$. This algorithm systematically divides isopleths, which systematically partitions the wind field into numerous marching squaresand utilizes grid cells (squares) and employs a divide-and-conquer strategy to determine the intersection points at which the wind exact intersection points where the flow transitions from easterly to westerlydirections (Lorensen, 2020). The

A schematic illustration of the method used to identify vortex centers is provided in Fig. 1illustrates a potential anticyclone center , denoted by the blue open circle, which corresponds to the location of maximum in Montgomery, ψ. The . Each potential anticyclonic vortex center corresponds to a local maximum in MSF along the $u = 0$ contour (bold black lineindicates the contour line where). Because the $u = 0$, which intersects the center of the anticyclone. The regular grid points represent the data points derived from the reanalysis data. It is evident that the $u = 0$ contour line does isopleths do not align perfectly with the grid points of the reanalysis data. Consequently, certain points in $u = 0$ isopleth require interpolation utilizing discrete reanalysis grid, the location of the contour and the values of MSF along it are determined using linear interpolation between the two nearest data points ; for grid points in the meridional direction. For instance, the data represented by value of MSF at the blue open circle necessitates interpolation would be linearly interpolated from the adjacent upper and lower points , indicated by the red and blue dots, respectively.

The scheme for identifying the vortex center and filtering out the spurious centers. The candidate vortex is represented by blue circle which locates at the maximum MSF, the reanalysis grid point closes to the candidate centre is indicated by a blue filled dot. The four renanalysis grid points closest to this closest point (the blue dot) are indicated by blue crosses. The black solid line is the contour of u = 0, the gray ellipse is the large area of anticyclone, the shading coral ellipse is the core of

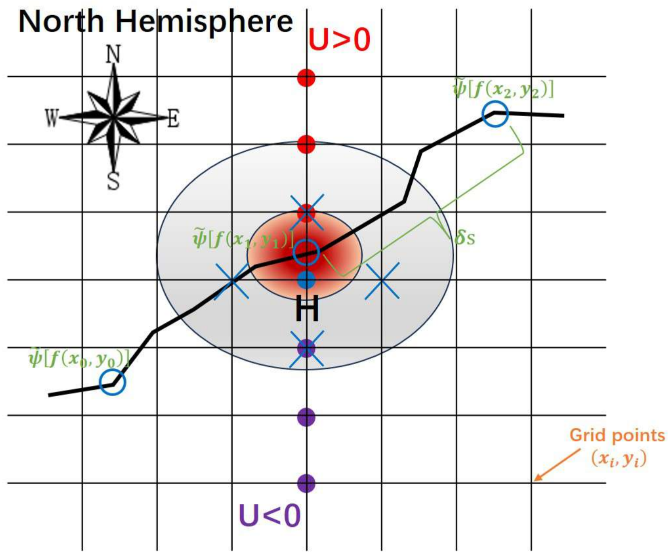

Figure 1. Schematic illustration of the method used to identify vortex centers and filter out spurious centers. The candidate vortex center, which marks a local maximum in Montgomery stream function (MSF) along the $u = 0$ ridgeline, is represented by the open blue circle co-located with the maximum MSF, while the reanalysis grid point closest to the candidate centre is indicated by a filled blue circle. The four reanalysis grid points directly adjacent to this closest point are indicated by blue crosses. The black solid line illustrates the $u = 0$ contour, the gray ellipse illustrates the area of the anticyclonic vortex, and the shaded coral ellipse illustrates the core of the anticyclonic vortex. In the Northern Hemisphere, we require relative vorticity $\zeta < 0$ at the central five points (blue filled circle and blue crosses), westerly wind anomalies at the three grid points located poleward of the central point (red filled circles), and easterly wind anomalies at the three grid points equatorward of the central point (purple filled circles). Adapted from Figure 5 of Siu and Bowman (2020).

anticyclone. In northern hemisphere, the relative vorticity $\zeta < 0$ and the three grid points located poleward/equatorward of the nearest grid point must exhibit westerly/easterly winds, as denoted by red/purple dots, respectively. This scheme is re-organized based on Figure 5 of .

After finding one or more sets of zero-zonal wind ($u = 0$) contours within the specific domain, the next step is to locate the vortex centers, if they exist, along these zero-zonal wind contours. The MSF along the zero-zonal wind isopleths does not pass through the grid points of the reanalysis data perfectly, and also need to be interpolated by the two nearest points. And the interpolated Montgomery, $\tilde{\psi}$ is the function of grid coordinates, (x_i, y_i) which can be expressed as

$$\tilde{\psi}[f(x_i, y_i)] = \tilde{\psi}(s_i)$$

where s_i is the distance along the contour, e.g. from point (x_{i-1}, y_{i-1}) to (x_i, y_i), calculated as the aggregate of the poleward and equatorward grid points (the closest red dot and the blue dot, respectively). MSF values along the contour are treated as a function of path distance s_i, computed as the cumulative great-circle arc lengths corresponding to the contoursegments, f

represents the map function that maps (x_i, y_i) to s_i. For each set of contours, a local maximum of $\tilde{\psi}(s_i)$ is identified within the specified range of $s_i - \delta s \leq s_i \leq s_i + \delta s$, where δs is length from a reference point on the contour. Local maxima of MSF along the ridgeline are required to be unique within a span of length $2\Delta s$ around s_i ($s_i \pm \Delta s$), where Δs is a half-angle search windowthat $\delta s = R\delta a$, and δa is . Following Siu and Bowman (2020), we set the central angle of the great-circle arc which is chosen to be $7.5°$ through , R is the Earth radius . The minimum allowable distance between two adjacent peaks of $\tilde{\psi}$ (to $\Delta a = \Delta s / R_e = 7.5°$, where R_e is the average radius of the Earth. The distance Δs thus also defines the minimum allowable separation between adjacent peaks (candidate vortex centers) along a contour is denoted as δs, and the quantity of distinct vortices identified may fluctuate over time.

Furthermore, it is crucial to filter out vortices that may arise the ridgeline. To exclude 'spurious centers' arising from small-scale features or from noise inherent in the gridded data, which these vortices are so called "spurious center". noise or localized features, we apply three filtering criteria:

1. Vorticity sign: The relative vorticity , ζ at the central grid point (indicated by the blue dot) identified center and its four nearest grid points (represented by blue crosses) within the reanalysis grid is characterized as anticyclonic should be less than 0 ($\zeta < 0$) in Northern Hemisphere. Also, the must be anticyclonic (i.e. $\zeta < 0$ in the Northern Hemisphere).

2. Zonal wind direction: The three grid points located poleward and equatorward of the central grid point must be westerly zonal wind immediately poleward of the center must be characterized by westerly flow ($u > 0$, red dots)and easterly zonal wind), while the three points equatorward must be characterized by easterly flow ($u < 0$, purple dots), respectively. The minimum length ().

3. Contour length: The corresponding $u = 0$ contour must occupy a minimum great-circle arc distance) of each set of contours should be greater than $2R\delta a$ length greater than $2R\Delta a$ (Siu and Bowman, 2020). The last step is to differentiate the persistence and dynamics of sub-vortices over timeby conducting a series of vortex analyses at various temporal intervals. The vortices are classified as "persistent", if the location of a vortex center remains stable within a threshold of $10°$ of

The final step in the algorithm is to track the movement and duration of each vortex center over time. To do this, we repeat the same vortex-tracking analysis at 6-hourly intervals. A vortex is classified as "persistent" (long-lasting) if two conditions are met. First, the vortex center must move no more than $10°$ along the Earth's surface (measured as great-circle distanceand exhibits continuity for a minimum of 18 hours, the remaining vortices are characterized as "transient") between one time step and the next. Second, the vortex must remain visible (continuous) for at least four time steps (i.e. ≥ 18 hours total). Any identified vortices that do not meet these conditions are designated as "transient" (short-lived) vortices (Siu and Bowman, 2020). All the processes of vortex tracking are carried out tracking procedures are performed using u, MSF, and ζ on the 370 K isentropic surface.

3.2 PV tendency diagnostic

To quantify the multi-center structure, zonal propagation, and intensification of the ASMA on isentropic surfaces, this study employs we develop a combined diagnostic based on the MSF, PV, and PV tendency. Each quantity plays a distinct and complementary role in the anticyclonic circulation in the UTLS. The evolution of the upper-level anticyclone. MSF provides a dynamically consistent field for identifying anticyclonic centers on isentropic surfaces. Unlike geopotential height on pressure levels, the MSF directly incorporates both thermal and Analogous to geopotential on pressure surfaces, MSF defines streamlines of geostrophic wind on isentropic surfaces. However, unlike geopotential, MSF incorporates local thermal contributions in addition to column-thickness dynamical contributions. The MSF is used to identify and track multiple ASMA centers along the zero zonal-wind contour simultaneously, following the approach of Siu and Bowman (2020) , thereby enabling a characterization as outlined above. This component enables objective identification of persistent and transient anticyclonic modes. According to the definition of MSF from :

$$\psi = C_p T + \mathrm{g} z,$$

where C_p is the specific heat at constant pressure of dry air, T is the temperature of the air on the isentropic surface, g is the gravitational acceleration, and z is geopotential height of the isentropic surface. While the MSF is used to locate and track ASMA centers, potential vorticity is employed to quantify the strength , spatial extent, and dynamical coherence of the anticyclonic circulationWe use PV to evaluate the strength and coherence of each vortex. PV is particularly especially advantageous in the UTLS because it is conserved under adiabatic and frictionless conditionsand therefore provides , providing a physically meaningful measure of vortex evolution (Hoskins et al., 1985). In this study, PV diagnostics are applied on the 370 K isentropic surface, which approximately corresponds to the climatological ASMA core. The local rate of change that is the isentropic density of pressure p with potential temperature θ can be expressed First, we define the isentropic mass density σ (the inverse of static stability) as:

$$\sigma = -g\mathrm{g}\frac{\partial p}{\partial \theta}. \tag{1}$$

Also, the ψ has a relationship with p and has a formula by Exner function :

$$\frac{\partial \psi}{\partial \theta} = C_p \left(\frac{p}{p_0}\right)^{\frac{R_d}{C_p}}$$

where p_0 is a standard reference surface pressure, usually taken as 1000 hPa, R_d is the specific heat at constant pressure of dry air. Based g is the gravitational acceleration and p is pressure. Building on the momentum and continuity equations on the isentropic surface . Then isentropic surfaces (Andrew et al., 1986), we use PV to diagnose the locationboundaries, area, and strength of the anticyclone at 370 K isentropic leveleach anticyclonic vortex. Under a hydrostatic and small-slope approximation, the simplified Ertel's PV under a small slope and a hydrostatic approximation 's PV is defined as:

$$q\mathrm{PV} = \frac{(\zeta+f)}{\sigma}\frac{(\zeta_\theta+f)}{\sigma} = -g\left(\zeta_\theta+f\right)\frac{\partial\theta}{\partial p} \tag{2}$$

where ζ is relative vorticity, ζ_θ is the relative vorticity perpendicular to the isentropic surface and f is the planetary vorticity . The PV framework is a powerful tool to explain the development and dissipation of ASMA, particularly useful on the quantity conserved adiabatic-frictionless flow . The Ertel's PV in pressure coordinate is defined as (Ertel, 1942; Charney, 1948).

$$q = -\mathrm{g}\left(\zeta+f\right)\frac{\partial\theta}{\partial p} + \mathrm{g}\left(\frac{\partial v}{\partial p}\frac{\partial\theta}{\partial x} - \frac{\partial u}{\partial p}\frac{\partial\theta}{\partial y}\right)$$

u and v are zonal and meridional wind, $\zeta = \partial v/\partial x - \partial u/\partial y$. Although instantaneous PV fields can effectively describe the structure of the ASMA, they do not directly distinguish between changes arising from vortex intensification and zonal propagationor background PV evolutionincluding sub-vortices, they cannot directly distinguish changes driven by intensification from those driven by propagation. To address thislimitation, we analyze the PV tendency, which explicitly quantifies the processes responsible for temporal changes in PV . By decomposing the PV tendency into dynamical and thermodynamical contributions, this approach allows the separation of anticyclonic strengthening from eastward or westward propagation to understanding ASMA multimodality.The term q is a nonlinear function of winds and potential temperature. The over time. Assuming friction is negligible for the large-scale UTLS flow, the PV tendency is approximated to as the sum of dynamic and thermodynamic terms if the frictions is negligible, we have

(advective) and thermodynamic (diabatic) terms:

$$\frac{\partial q}{\partial t}\frac{\partial \mathrm{PV}}{\partial t} = -u\frac{\partial q}{\partial x}\frac{\partial \mathrm{PV}}{\partial x} - v\frac{\partial q}{\partial y}\frac{\partial \mathrm{PV}}{\partial y} - w\frac{\partial q}{\partial p}\dot{\theta}\frac{\partial \mathrm{PV}}{\partial \theta} + Q_\theta \tag{3}$$

where t is time, w is vertical velocity at each level, Q is $\dot{\theta}$ is the (diabatic) vertical velocity in potential temperature coordinates and Q_θ represents the PV tendency from total diabatic heating including the temperature tendency due to moist process (latent heating) Q_{LH}, solar or longwave radiative heating, and friction etc. The friction termis negligible for the large-scale flow. Also, the PV tendency can be decomposed into a background flow component that represents the climatological mean (including both radiative and non-radiative processes). Keeping only the vertical component of the diabatic source term, we have:

$$Q_\theta \equiv \mathrm{PV}\left(\frac{\partial\dot{\theta}}{\partial\theta}\right) \tag{4}$$

To further clarify the drivers of ASMA variability, we decompose the flow into a time-mean zonal-mean background flow ($\bar{\varphi}$) and a perturbation component that accounts for anomalies. It is assumed that the decomposition is time-independent and exhibits zonal symmetry. Consequently, for the purpose of this analysis, $a(x,y,p,t) = \overline{a(y,p)} + a'(x,y,p,t)$ where a is any field of interest like u, v, w flow (φ'), such that $\varphi(x,y,p,t) = \overline{\varphi(y,p)} + \varphi'(x,y,p,t)$ (Tamarin and Kaspi, 2016), and the $\overline{a(y,p)}$ is the time and zonal mean. The meridional background flow represents a contribution to the PV tendency that is an order of magnitude smaller, so the PV tendency equation can be decomposed into mean and anomaly to gain better insight into variation in ASMA intensification:

. The PV tendency equation can then be expanded to highlight variations in intensification:

$$\frac{\partial q}{\partial t}\frac{\partial \mathrm{PV}}{\partial t} = \frac{\partial q'}{\partial t} = \frac{\partial \mathrm{PV}'}{\partial t} \approx -\bar{u}\frac{\partial q'}{\partial x}\frac{\partial \mathrm{PV}'}{\partial x} - v'\frac{\partial \bar{q}}{\partial y}\frac{\partial \overline{\mathrm{PV}}}{\partial y} - u'\frac{\partial q'}{\partial x}\frac{\partial \mathrm{PV}'}{\partial x} - v'\frac{\partial q'}{\partial y}\frac{\partial \mathrm{PV}'}{\partial y} - w\frac{\partial q}{\partial p}\dot{\theta}\frac{\partial \overline{\mathrm{PV}}}{\partial \theta} - \dot{\theta}\frac{\partial \mathrm{PV}'}{\partial \theta} - \left(\overline{\mathrm{PV}} + Q\mathrm{PV}'\right)\frac{\partial \dot{\theta}}{\partial \theta} \quad (5)$$

Here, the $-\bar{u}\partial q'\partial x$ $-\bar{u}\partial \mathrm{PV}'/\partial x$ represents the advection of the PV perturbation by the background zonal mean flow , the $-v'\partial \bar{q}/\partial y$ term flow (referenced as 'mean zonal advection'), while $-v'\partial \overline{\mathrm{PV}}/\partial y$ is the meridional advection of the background vorticity PV by the perturbation velocity associated with anticyclone. The next two terms $-u'\partial q'/\partial x$, $-v'\partial q'\partial y$ represents the nonlinear perturbation advectionterms, ('meridional mean advection'). The terms $-u'\partial \mathrm{PV}'/\partial x$ and $-w\partial q/\partial p$ represents the vertical advection $-v'\partial \mathrm{PV}'/\partial y$ are collectively referred to as 'nonlinear horizontal advection', with $-\dot{\theta}\partial \mathrm{PV}/\partial \theta$ representing total diabatic vertical advection (without decomposition). The time-mean background flow along the ridgeline is defined to be zonal ($\bar{v} = \partial \overline{\mathrm{PV}}/\partial x = 0$) and adiabatic ($\dot{\theta}' = \dot{\theta}$), under the assumption that the horizontal scale of the ASMA is large relative to the tracked vortices.

However, on an isentropic surface (like the 370 K surface), the potential temperature θ is constant by definition. This means the horizontal gradients of θ are zero: $\partial\theta/\partial x = 0$ and $\partial\theta/\partial y = 0$. Therefore, the second term (the tilting term)vanishes, and the expression simplifies to:

$$q = -\mathrm{g}\left(\zeta_\theta + f\right)\frac{\partial \theta}{\partial p}$$

where ζ_θ is the relative vorticity calculated using winds on the 370 K surface. The rate of change of PV We adopt potential temperature coordinates for analysis due to the wind blowing different values of PVacross the point. Here, u and v are the eastward and northward wind components on the 370 K surface, and $\partial q/\partial x$ and $\partial q/\partial y$ are the horizontal gradients of PV on that same surface. This is typically the dominant term. And the distinct advantages for studying upper-tropospheric dynamics, particularly those related to PV (Hoskins et al., 1985). Isentropic surfaces, which are defined as surfaces of constant potential temperature θ, are intrinsically aligned with adiabatic air parcel motion. This alignment simplifies interpretation of PV evolution because PV is conserved under adiabatic, frictionless conditions, making it easier to track air mass movement and isolate the key dynamical and thermodynamic mechanisms driving ASMA variability. In addition, this coordinate system simplifies the vertical term, as the adiabatic component of vertical motion is wrapped into the horizontal advective terms. The local rate of change of PV due to air moving vertically across on the 370K surface (diabatic motion) where a vertical gradient of PV($\partial q/\partial\theta$)exists. The PV tendency equation on 370 K is K isentropic surface is thus governed primarily by horizontal advective transport of PV, modified by diabatic transport and diluted by diabatic vertical convergence, as expressed in Eq. (5).

$$\frac{\partial q}{\partial t} = -u\frac{\partial q}{\partial x} - v\frac{\partial q}{\partial y} - \dot{\theta}\frac{\partial q}{\partial \theta} + Q_\theta$$

where $\dot{\theta} = d\theta/dt$ is the diabatic heating rate (e.g., from latent heat release or radiation). Q_θ is diabatic heating, the source/sink term that generates or destroys PV through differential diabatic heating One key uncertainty concerns the assumption of frictionless flow, as convective momentum transport, gravity wave drag, and shear-flow instability could all modify the flow near the monsoon tropopause. Assimilation effects on winds and temperatures can also be locally large in reanalyses, especially in the vicinity of complex topography such as the Tibetan Plateau (e.g. Wright et al., 2025). However, these effects are often tied to topography and therefore difficult to interpret and potentially confounding in a vortex-relative framework such as the one adopted here. We center our analysis around the model-generated diabatic heating terms to better attribute these contributions and their consistency across reanalyses, and defer a more complete accounting of assimilation effects and parameterized momentum sources and sinks to future work.

4 Vortex tracking and PV tendency analysisresults

4.1 Movementsof vortex centers within the ASMA

The MSFMontgomery stream function (MSF), relative vorticity, and zonal wind are involved in the multi-center vortex tracking of ASMA , the tracking domain is 0°– 180°E and 15°– 45°N in the period of 2000–2020. Figure2 shows the vortex tracking on used to identify and track multiple vortex centers within the ASMA over the domain 0°-180°E and 15°-45°N during the period 2000–2020. Figure 2 shows an illustrative example of vortex identification on the 370 K isentropic surface by the method as discussed in section 3. Figure2 reveals arelationship between zonal wind $u$using the method described in Section 3. Figure 2 highlights the dynamical consistency among potential vorticity (PV; Fig. 2a), relative vorticity (ζ; Fig. 2b), and MSF ψ, the vortex center locates at the intersection of maximum ψ and zero-zonal wind line, with $\zeta < 0$.Figure S1 shows the and zonal wind (u; Fig. 2c). Vortex centers are identified at locations where MSF reaches a local maximum along the $u = 0$ ridgeline. These vortices are likewise characterized by negative relative vorticity ($\zeta < 0$) and small values of PV. The typical number and frequency of occurrence of ASMA ASMA vortex centers from May to August . The centroid locations agree well among three reanalysis data, even the results by are shown in Fig. 3 for JRA-3Q, with results for other reanalyses shown in Fig. S1 of the supporting information. The most frequent centroid locations are consistent across the three reanalysis products, with JRA-3Q and ERA5 are much closer.The three modes are obvious in frequency-longitude histogram, the Iranian Plateauagreeing particularly well (Fig. S1; see also Fig. 3). The longitude–frequency distribution (Fig. 4) shows three distinct modes: an 'Iranian Plateau' (IP) mode near 50°E, Tibetan Plateau a 'Tibetan Plateau' (TP) mode near 90 E, and Western Pacific 90°E, and a 'Western Pacific' (WP) mode around 135°- 150°E which are similar to and . These three modes are often

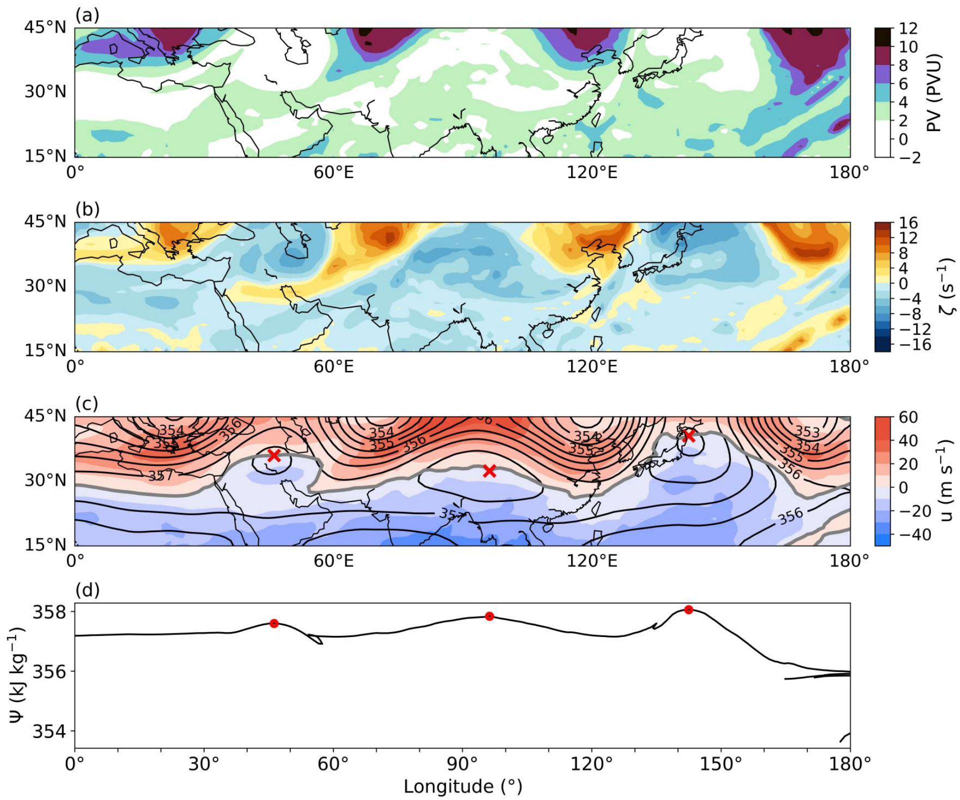

Figure 2. An illustrative example of vortex center identification ~~of~~ in the ASMA region based on JRA-3Q products at 370 K on ~~UTC 00:00 August~~ 17~~, 2019.~~ August 2019 at 00UTC: (a) potential vorticity, PV~~(q)~~; (b) relative vorticity, ζ; (c) zonal wind, ~~u~~u, including the zero-wind ~~,~~ $u = 0$ ~~contour~~ ridgeline (gray line) ~~, the~~ as well as identified vortex centres (red crosses), ~~the MSF, ψ~~ and Montgomery stream function (MSF; black ~~contour~~contours); and (d) MSF along the ~~zero-wind line versus~~ $u = 0$ ridgeline as a function of longitude, along with the ~~corresponding~~ identified vortex ~~center~~ centers (red dots).

.

~~referred~~ at 135°–150°E, in agreement with previous studies (Honomichl and Pan, 2020; Siu and Bowman, 2020). These modes correspond to the Iranian, Tibetan, and Bonin (Ogasawara) highs (Enomoto et al., 2003; Enomoto, 2004)~~, also the relationship between .~~. The TP and WP ~~high is often referred to as South Asian high,~~ modes are often collectively associated with the South Asian High, while the IP and TP ~~mode also have an interaction relationship with the spatial distribution of Fig. S1, some WP modeare caused by~~ modes exhibit clear spatial interaction (e.g. Zhang et al., 2002; Nützel et al., 2016; Zhang et al., 2025). Moreover, part of the WP mode, which occurs mainly later in the monsoon season, can be linked to eastward eddy shedding. As shown by Nützel et al. (2016)~~have found~~ , the occurrence frequencies of the IP and TP modes are concentrated within 25°-35°N ~~, 45°–100°E, and~~ and 45°-100°E. Siu and Bowman (2020) ~~find an expansive area of frequent in~~ also highlighted a broad region of frequent vortex occurrence associated with the Bonin High (BH) ~~between 120°–180°E, these vortices are~~ over

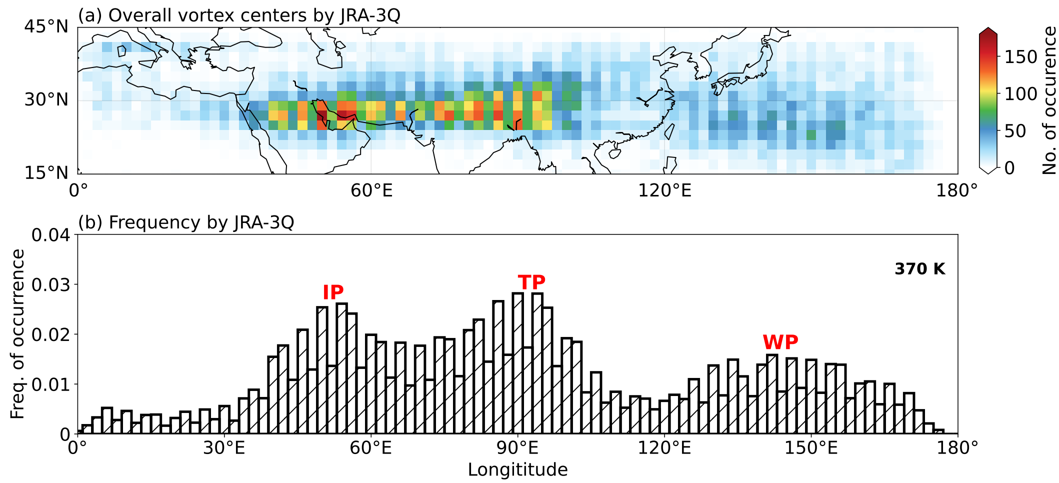

Figure 3. The spatial distributions of occurrence frequency of the anticyclone centers on the 370 K isentropic based on JRA-3Q during May–September 2000–2020. The red ‘IP’ in (b) marks peak associated with the Iranian Plateau mode, ‘TP’ marks the Tibetan Plateau mode, and ‘WP’ refers to the Western Pacific mode.

120°-180°E, where vortices are generally weaker than those ~~in TP and IP . Our results of vortex tracking~~ defining the IP and TP modes. Overall, the vortex tracking results presented here are consistent with ~~the above puiblications both in distribution and histogram~~previous studies in both spatial distribution and frequency characteristics.

~~To enhance our understanding of the variations in the ASMA~~

To gain a better understanding of ASMA variability, particularly the ~~observed trimodality~~ pronounced trimodal structure from May to September, ~~we plot Hovmöller diagrams~~ Hovmöller diagrams are constructed to illustrate the spatiotemporal evolution of vortex ~~movements. It shows the locations of the anticyclone relating to time , latitude, and longitude~~centers. These diagrams depict the densities of longitudinal and latitudinal positions of anticyclonic vortices within the ASMA as a function of time of year. The trimodal structure ~~,~~ comprising the IP, TP, and WP modes is ~~obvious~~ clearly evident in panels (a)-~~-~~(c) of Fig.~~3. The detailed~~ 4. The longitudinal ranges of the vortex centers ~~can be identified, with the climatological centers of~~ are well defined, with climatological centers for the IP, TP, and WP modes located at approximately ~~45°–65°E, 85°–100°E, and 135°–145°E~~45°-65°E, 85°-100°E, and 135°-145°E longitude, respectively. ~~Additionally, the~~ The relative prevalence of these three centers likewise shows a clear seasonal evolution, with the TP center dominant during May, IP from mid-June to mid-July, and a shift back to predominantly TP centers as the BH emerges in August and September. The ASMA exhibits a ~~strong latitudinal dependency for both persistent and transient type that the anticyclone moves northward (slightly) during the beginning of boreal summer and southward later, then reaching its north latitude~~ clear latitudinal evolution of vortex centers as well, with a northward migration of vortex density in early boreal summer followed by a southward migration later in the season. The northernmost position of approximately 40°N ~~between July~~ is reached between 15~~and August~~ July and 14~~, which is similar to results. The persistent vortex identified by~~ August. This behavior is likewise consistent with previous findings

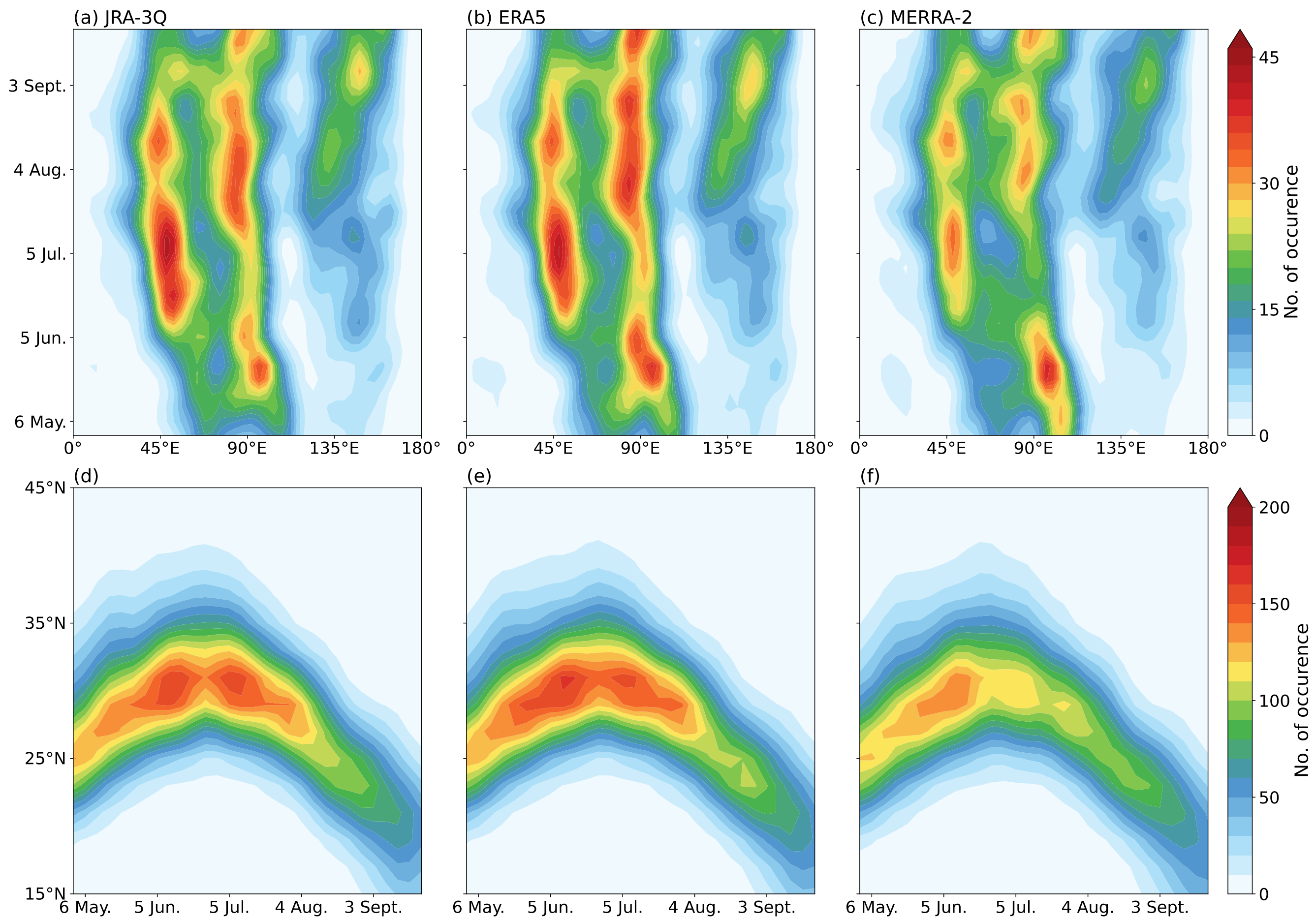

Figure 4. Evolution of vortex occurrence counts based on applying the vortex tracking algorithm at 370 K level from 2000 to 2020 in the (a)–(c) time–longitude and (d)–(f) time–latitude phase spaces. Results are shown for the (a),(d) JRA-3Q, (b),(e) ERA5, and (c),(f) MERRA-2 reanalysis products.

(Nützel et al., 2016, 2022). Persistent vortices account for more than 65% of identified vortex centers in ERA5 and JRA-3Q~~reanalysis constitutes over 65% of the overall vortex centers, while the transient vortex is relatively rare comparing to the persistent vortex, as illustrated in Table~~, while transient vortices occur much less frequently (Table S1~~.~~).

~~Figure 4 shows the~~

Figure 5 shows four examples of anticyclone ~~movements from May to September in~~ evolution during May–September of the years 2000, 2005, 2010, 2015, and ~~2020, respectively, where the PV fields during the summer on the isentropic surface at~~ 2020. The panels show PV fields on the 370~~K~~ K isentropic surface, with color shading ~~values~~ ranging from 0 to 2~~PVU. The low PV patterns observed in the~~ PVU. Low-PV structures in JRA-3Q ~~exhibit a high degree of consistency~~ are highly consistent with the locations of ~~anticyclone. Additionally, most of the features of anticyclone moving westward and eastwardcoexisted with~~

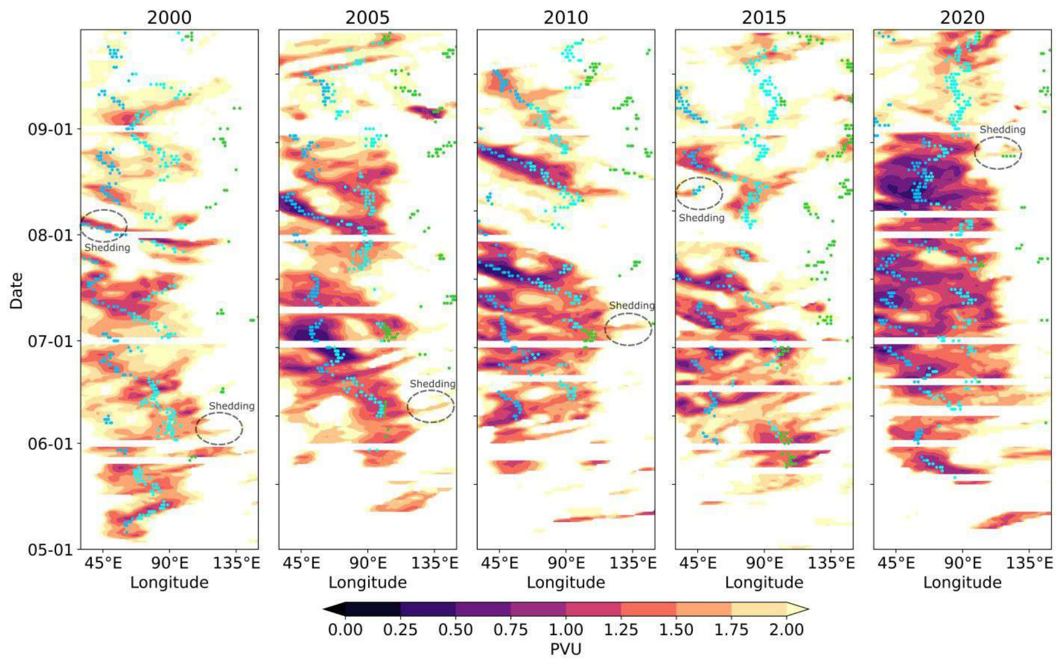

Figure 5. Time–longitude plots of 6-hourly PV at 370 K over the latitudinal band between 20°N and 40°N in 2000, 2005, 2010, 2015, and 2020 based on JRA-3Q. Light blue, cyan, and green dots represent the locations of persistent anticyclonic vortex centers in the IP, TP, and BH regions, respectively. Grey dashed circles mark exemplary eddy shedding events.

~~the almost stationary low PV area, and these are actually~~ the identified anticyclone centers. Many anticyclonic features show evidence of westward propagation, although some features propagate eastward, especially in the early and late monsoon, and periods of long-lasting quasi-stationary centers are also evident (e.g. August 2020). Tails extending toward both the eastern and western boundaries indicate eddy shedding events (Popovic and Plumb, 2001)~~, also the vortices have relative larger PV in September.The western Pacific is located in~~ . There remains no universally accepted quantitative threshold for defining eddy shedding in the ASMA, as it involves gradual vortex splitting, detachment, and westward/eastward propagation that is inherently continuous and difficult to discretize objectively. We therefore mark only a handful of typical, visually clear cases to illustrate eddy shedding behavior in Fig. 5, rather than attempting to label every event. The Western Pacific sector lies within the southward-flowing, eastward flank of the anticyclone, ~~which transports~~ where high-PV air from the extratropical lowermost stratosphere ~~equatorward, which may lead to larger PV~~ is often advected toward lower latitudes. This southward mean advection contributes to the enhanced PV there (Wang et al., 2022). Although ~~the vortices mainly move in the east-west direction or shedding, movement in the north-south direction can also occur~~vortex motion is predominantly zonal (east–west), many vortices also experience meridional (north–south) displacements during their life cycles (not shown).

~~The evolution of vortex occurrence counts by vortex tracking at 100 hPa from 2000 to 2020 in (a, b, c) time-longitude and (d, e, f) time-latitude plots. Shown are (a, d) JRA-3Q, (b, e) ERA5 and (c, f) MERRA-2 reanalysis results~~

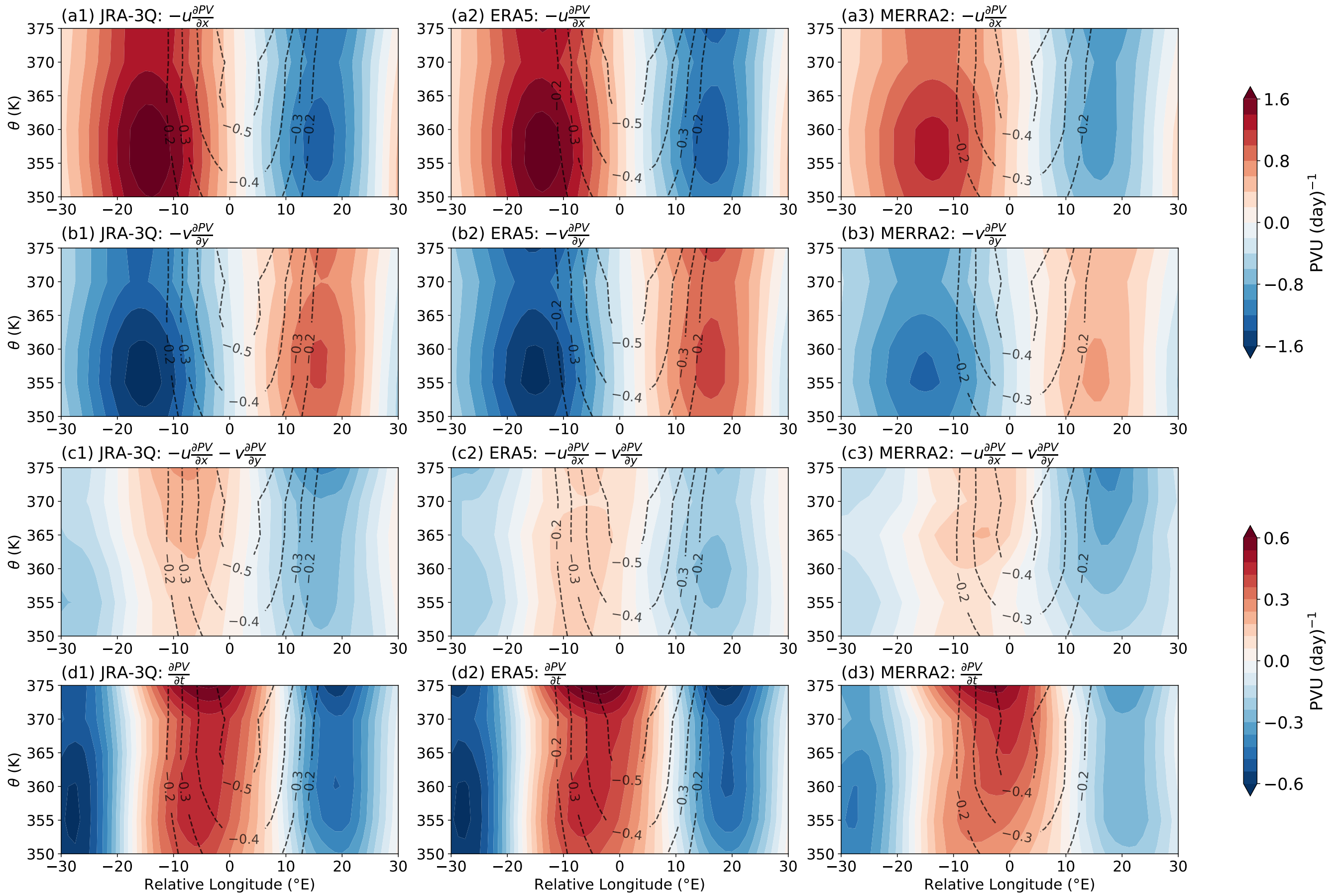

Figure 6. Composite-mean PV tendencies from (a) zonal advection ($-u\partial \mathrm{PV}/\partial x$), (b) meridional advection ($-v\partial \mathrm{PV}/\partial y$), (c) the sum of zonal and meridional advection, and (d) the net time tendency ($\partial \mathrm{PV}/\partial t$). PV anomalies are shown as black dashed contours at 0.1 PVU intervals from -0.2 to -0.5 PVU. The horizontal axis indicates the longitude relative to the vortex center. Results are shown for the (a1-d1) JRA-3Q, (a2-d2) ERA5, and (a3-d3) MERRA-2 reanalysis products.

4.2 Development of vortex centers within the ASMA

~~Time-longitude plots of 6 hourly PV at 370 K over the latitudinal band between 20°N and 40°N in 2000, 2005, 2010, 2015 and 2020 (from JRA-3Q). The light blue, cyan, and green represents the locations of persistent anticyclone over IP, TP, and BH regions. The gray and dashed circle indicates the eddy shedding events.~~

4.3 ~~Development process of the ASMA~~

~~The vertical cross section from~~ Figure 6 shows vertical cross-sections for each term in Eq. (~~??)are calculated separately in each term and shown in Fig. 5 and the longitudinal and latitudinal extents are set of ±30° and ±15° from the center of~~

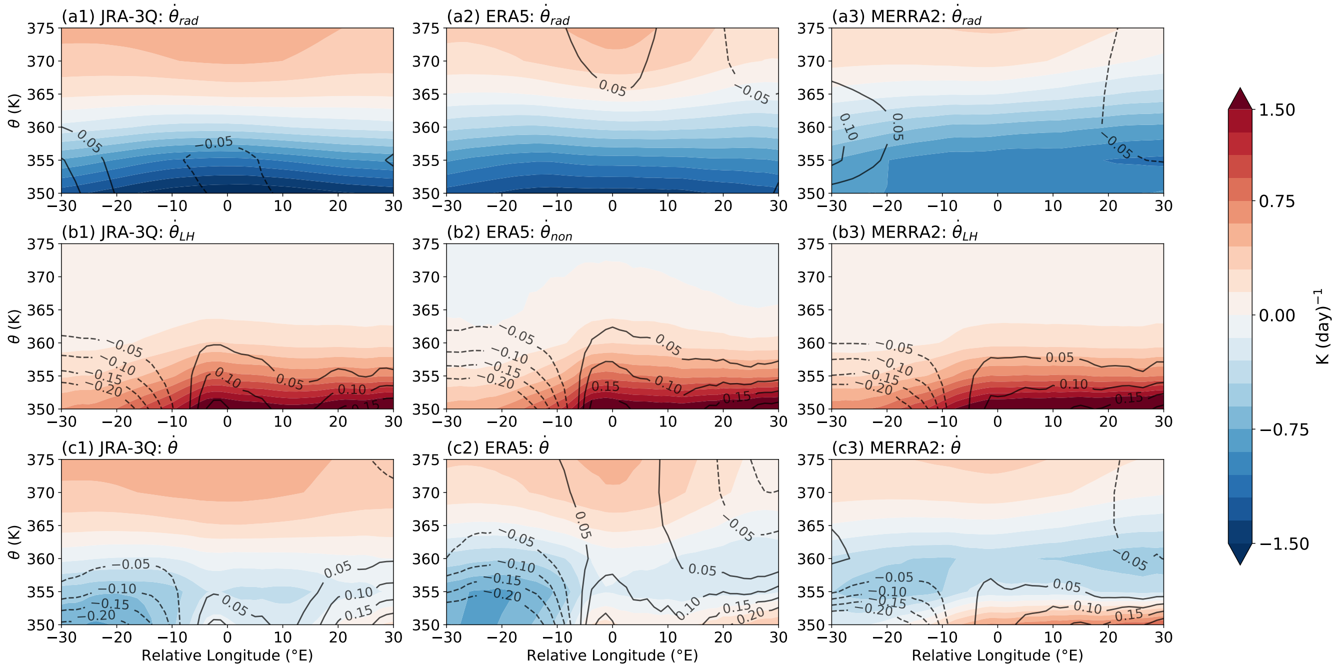

Figure 7. Composite-mean diabatic vertical velocities ($\dot{\theta}$) due to (a) radiation, (b) latent (JRA-3Q, MERRA-2) or non-radiative (ERA5) heating, and (c) all parameterized physics based on the (a1-c1) JRA-3Q, (a2-c2) ERA5, and (a3-c3) MERRA-2 reanalyses. The horizontal axis indicates the longitude relative to the vortex center. Contour lines show differences relative to the zonal mean across the eastern hemisphere (0°–180°E).

~~anticyclone. The~~ 3). The extents are defined as ±30° in longitude and ±15° in latitude relative to the center of the vortex. A dipolar structure of positive and negative ~~dipolar tendencies occur in Eq. (??), the $-u\partial q/\partial x$ and $-v\partial q/\partial y$ can cancel out approximately. The zonal advection of PV is more responsible for the positive PV tendency in the upper level (>~~PV tendencies is evident in both the horizontal advection terms (Fig. 6a-b). In the composite mean, zonal PV advection exhibits a positive tendency to the west and negative tendency to the east of the vortex center above 300 hPa~~), while the vertical advection leads to a positive PV tendency closed to the center of anticyclone and negative PV tendency remote from the center eastwardly. The contributions~~, while meridional advection is positive to the east and negative to the west. The dipoles thus largely cancel when the horizontal advection terms are summed together (Fig. 6c). The net time tendency of PV (Fig. 6d) is similar in structure to the sum of the horizontal advection terms, but with a larger amplitude. Both terms show a tripolar structure with positive tendencies immediately west of the vortex center flanked by negative tendencies to east and west.

Diabatic heating plays an influential role in setting the PV tendency and is essential for anticyclonic vortex development. The vertical structure of diabatic heating ~~that is dominated by the latent and radiative heating to the PV tendency are important for anticyclonic process. The association between the release of latent heating and the updraft motion of warm air in the anticyclone sector is illustrated in Fig. 5(e1)-(e3). Since latent heating is not explicitly provided in ERA5 data, a non-radiative~~

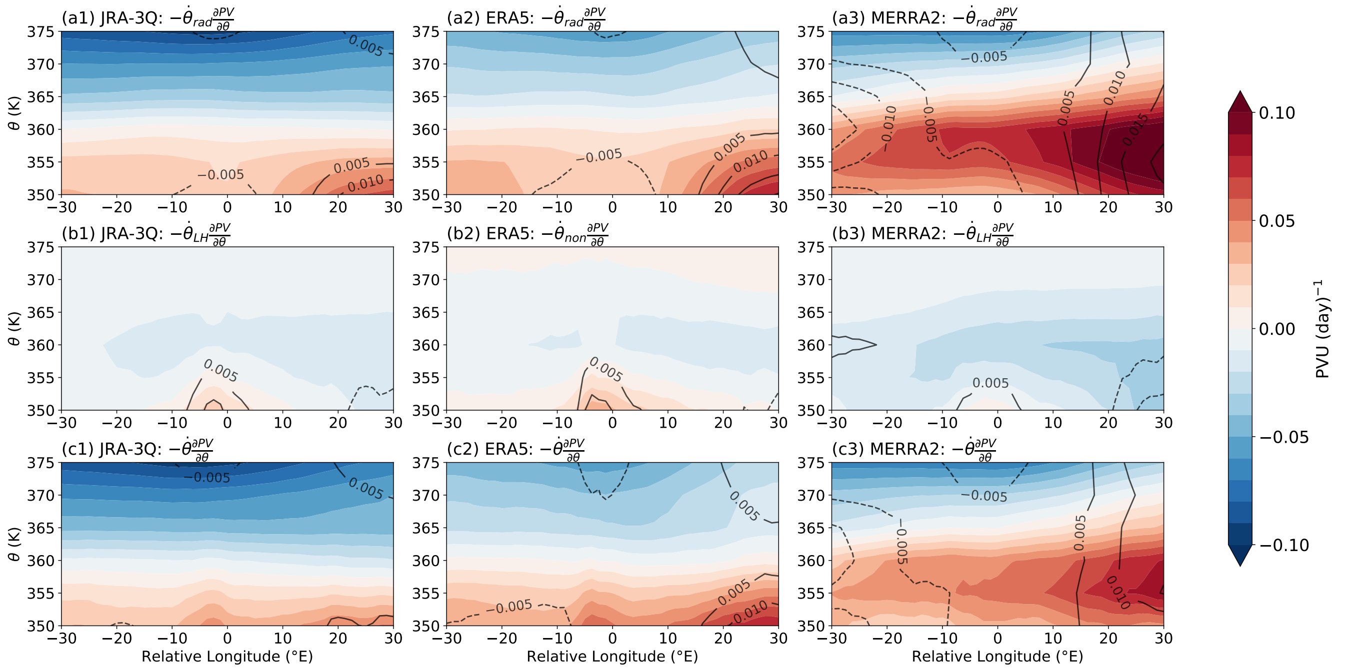

Figure 8. Composite-mean PV tendencies (shading; PVU day^{-1}) due to diabatic vertical advection of PV from (a) radiative heating, (b) latent or non-radiative heating, and (c) total diabatic heating based on the (a1-c1) JRA-3Q, (a2-c2) ERA5, and (a3-c3) MERRA-2 reanalysis products. Black contours show deviations from the background zonal-mean for the corresponding term. The horizontal axis indicates the longitude relative to the vortex center.

~~heating component dominated by latent heating~~ is ~~used here, which can reflect the characteristics of latent heating to a certain extent. As the warm and moist air travels upward, it cools and condenses, releasing latent heat, which produces positive PV tendency in lower level and negative PV anomaly and tendency in upper level. At the level higher than 200 hPa,~~ defined by a balance between latent heating and radiative cooling below about 360 K and dominated by radiative heating above this level. Figure 7 illustrates the distribution of diabatic heating around the identified anticyclonic vortices. On average, the identified vortices show strong deep convective heating collocated with the vortex center and below the eastern flank of the vortex, with much weaker heating below the western part of the vortex. Radiative heating in the upper levels also peaks near the center of the vortex, especially in ERA5 (Fig. 7a2). Strong radiative cooling in the lower levels compensates much of the positive anomaly in convective heating below 360 K, creating a band of negative net heating around 355–360 K that extends downward to 350 K in the western part of the vortex (Fig. 7c).

The contributions of diabatic heating to vortex evolution can be separated into two terms. The first of these corresponds to diabatic vertical advection, as shown in Fig. 8, and the horizontal slice on 370 K isentropic surface is detalied in Fig. S3. In this term, the ~~background radiation (longwave and shortwave heating) dominates the~~ diabatic heating distributions shown in Fig. 7 operate on the partial derivative of PV with respect to potential temperature. PV increases with height, with a local minimum at

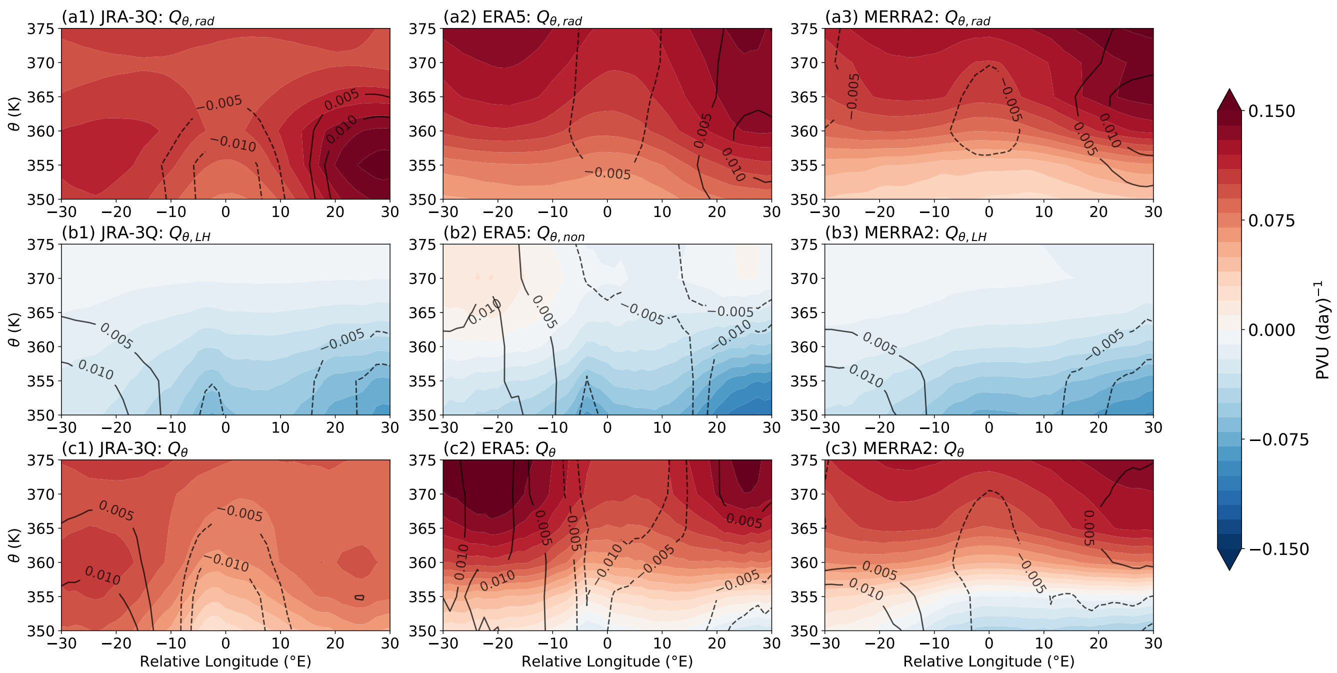

Figure 9. Composite-mean PV tendencies (shading; PVU day^{-1}) from the vertical divergence of (a) radiative heating Q_{rad}, (b) non-radiative heating Q_{non}, and (c) total diabatic heating Q based on the (a1-c1) JRA-3Q, (a2-c2) ERA5, and (a3-c3) MERRA-2 reanalysis products. Black contours show deviations from the background zonal mean for the corresponding term. The horizontal axis indicates the longitude relative to the vortex center.

the vortex center that is strongest in ERA5 and weakest in MERRA-2 (Fig. S2). As a result, upward vertical velocities tend to reduce PV and downward vertical velocities tend to increase PV. The net effect is a vertical dipole centered just below 360 K, with positive tendencies below and negative tendencies above this level. Whereas the qualitative structure is set primarily by the distribution of radiative heating, latent heating acts to shift the zero line downward. Further investigation shows that the positive tendency associated with latent heating near the vortex center results from collocation of the largest positive latent heating with a local reversal of the vertical gradient of PV.

Figure 9 shows PV tendencies induced by the vertical divergence of different diabatic heating components: radiative heating (Q_{rad}), latent (Q_{LH}; JRA-3Q and MERRA-2) or non-radiative heating (Q_{non}; ERA5), and total diabatic heating ~~, thus, resulting in positive PV tendency for cyclonic flow. The sum of each term in Eq.(**??**)shows a tripole PV tendency pattern, which is positive closed to~~ Q). The vertical divergence of radiative heating produces a strong positive tendency at these altitudes (Fig. 9a), primarily contributed by the increase in background radiative heating with increasing height (Fig. 7a). These tendencies indicate that the vertical structure of radiative heating in the UTLS, where tropospheric radiative cooling transitions to stratospheric radiative heating, generally acts to spin down the monsoon anticyclone through the diabatic source term. Beyond this general tendency, the spatial structure of radiative heating effects around the vortex center shows a stronger positive tendency in the eastern part of the vortex and a weaker positive tendency near the center of anticyclone and negative in eastward and westward. The findings from ERA5the vortex: the spin-down effect is less pronounced near the center of active anticyclonic vortices. Examination of Fig. 7, which shows that the composite mean vertical gradient of $\dot{\theta}$ is largest near the vortex center, indicates that this local minimum primarily reflects the local minimum in PV. By contrast to radiative heating, the decrease in latent heating near the tops of deep convective clouds produces negative PV tendencies that decrease in magnitude with increasing height (Fig. 9b). These negative tendencies show two peaks. The first is located near the center of the vortex, where it supplements the weaker positive radiative tendencies noted above. The second is located in the eastern sector of the vortex, where it offsets at least part of the stronger positive radiative tendencies. The net effect of the vertical divergence of diabatic heating (Fig. 9c) is to spin down the negative PV anomaly at higher altitudes, with stronger effects near the edges of the vortex and weaker effects near the center. The three reanalyses show large differences in the vertical locations of these effects and their relative magnitudes. Whereas positive tendencies in JRA-3Q , and peak near 360 K, positive tendencies in ERA5 and MERRA-2 exhibit minor discrepancies.Specifically, the potential temperature recorded in MERRA-2 is higher than that observed in increase with increasing height. Moreover, both ERA5 and MERRA-2 show negative tendencies in the lower part of this vertical range extending eastward from the vortex center. These differences may be explained by stronger anvil cloud radiative effects in ERA5 and MERRA-2 (Wright et al., 2020), which weakens the vertical gradient of radiative heating by producing positive longwave heating effects below the anvil and negative effects above the anvil (Fig. 7a). Like the earlier JRA-55 reanalysis, JRA-3Q across all levels. Additionally, the region characterized by PV anomalies, which indicates the core of the anticyclone, is also shown in Figproduces very little prognostic cloud ice at these altitudes (Zhang et al., 2025). Meanwhile, the gradient in diabatic source tendencies in MERRA-2 is considerably larger than those based on the other two reanalyses, owing to larger values of PV throughout this altitude range (Fig. S2 and S4 in the online supplement). 5.

The latent heat released during the formation of an anticyclone results in an expansion of the isentropes at higher altitudes while simultaneously causing a contraction of the isentropes at lower altitudes. This phenomenon leads to an increase in static stability at lower levels, thereby enhancing the potential temperature gradient, while the gradient diminishes at upper levels. The resultant warming effect elevates the geopotential height at higher altitudes, which in turn generates an outward pressure gradient force that induces divergence at these levels . This divergence facilitates upward vertical motion and convergence at lower altitudes, as illustrated in Fig. 5(c1)-(c3), ultimately contributing to an increase in potential vorticity.

Figure 6 shows the PV tendencies induced by different diabatic heating components—radiative heating (Q_{rad}), latent heating (Q_{LH}), and total diabatic heating (Q)which are

Figures 10 and 11 show latitude–longitude distributions of the diabatic source term on the 350 K and 370 K levels based on JRA-3Q, the same terms from ERA5 and MERRA2 are shown in Fig. S4 and S5. Results are shown separately for vortices associated with the IP, TP, and BH , three major modes of the ASMA. Background radiative heating (top row) produces positive PV Radiative heating (Fig. 10a-c) produces strong positive PV tendencies to the north of the anticyclone core , indicating that upper-tropospheric radiation acts to increase PV vortex core at 350 K, indicating an increase in radiative heating with increasing potential temperature acting to increase PV and weaken the circulation. In vortex. By contrast, latent heating (middle rowor non-radiative heating (Fig. 10d-f) generates strong negative PV PV tendencies south of the core, especially over the BH, where

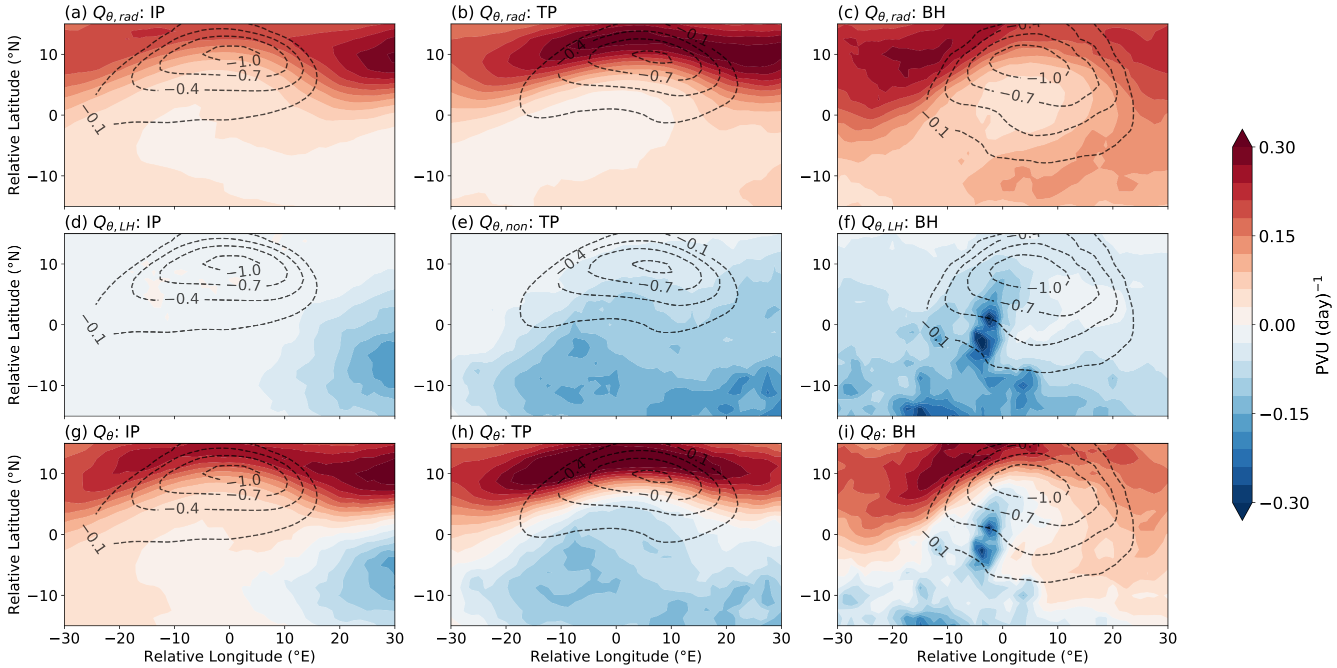

Figure 10. PV tendencies from the vertical divergence of (a)-(c) radiative heating, (d)-(f) latent or non-radiative heating, and (g)-(i) their sum on the 350 K isentropic surface based on JRA-3Q. Results are shown for the (a,d,g) Iranian Plateau (IP), (b,e,h) Tibetan Plateau (TP), and (c,f,i) Bonin High vortex modes. Black dashed contours show the PV anomaly at 350 K from -1 to 0 PVU at an interval of 0.3 PVU. The horizontal and vertical axes indicate longitude and latitude relative to the vortex center, respectively.

~~monsoonal convection and latent heat release are most intense. This PV reduction~~ vortex center. The associated reduction in PV enhances the anticyclonic vorticity and contributes to ~~ASMA intensification~~ vortex intensification or propagation. The total diabatic heating (bottom row), which combines both radiative and latent effects, shows a net negative ~~PV tendency around~~ PV tendency along the southern flank ~~of each high, the latent heating drives the strengthening of~~ the ~~ASMA, while radiative processes provide a weak damping influence, with the most pronounced diabatic enhancement occurring over the BH region. Additionally, this phenomenon is not so obvious in IP. Probably the IP differs in terms of the intensity of terrain dynamic forcing,~~ vortex and opposing effects along the northern flank. The orientation of this dipole between positive and negative tendencies differs between vortices associated with the IP, TP, and BH modes, primarily owing to differences in the latent heating component. Whereas the latent heating intensification is located in the ~~magnitude and concentration of diabatic heating (predominantly latent heat), the characteristics of large-scale circulation coupling, and the significant differences in the thermal properties of the underlying surface, it is still to be determined~~southeast for the IP mode, it is located in the south for the TP mode, and mainly to the southwest of the vortex center for the BH mode. Meanwhile, positive tendencies wrap around the western flank of IP-mode vortices and the eastern flank of BH-mode vortices. These distributions of the diabatic source term will tend to pull vortices in all modes back toward the southern flank of the central ASMA, where the convective core of

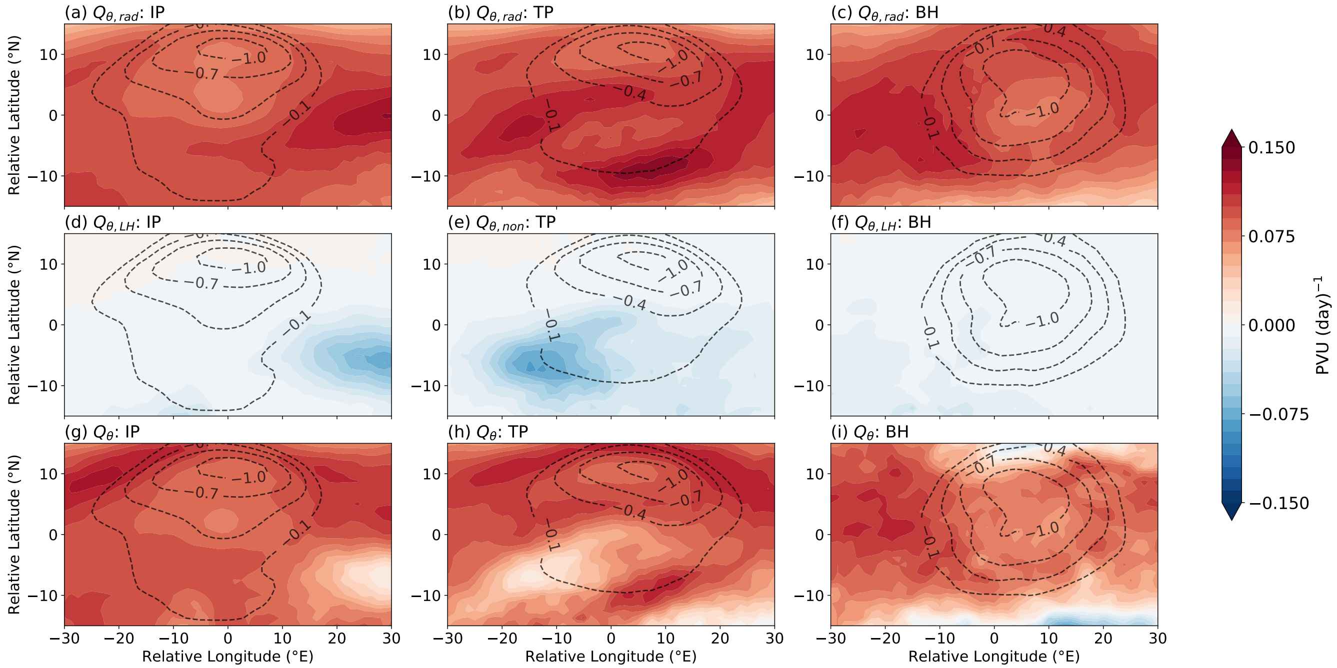

Figure 11. As in Fig. 10, but for the 370 K isentropic surface.

the monsoon is located and inhibit their propagation away from this center. It is important to note that these distributions are composite means over many vortex centers; the tendencies associated with individual vortices may differ.

~~Given that the tendency of PV is directly related to the product of absolute vorticity and~~

The dipole patterns shown in Fig. 10 are weaker on the 370 K level, as shown in Fig. 11. This difference largely results from a redistribution of the ~~rate of change in static stability, this process results in an increase in potential vorticity at lower levels and a decrease at upper levels. When examining the core of the anticyclone at 200 hPa, it is likely that~~ positive tendencies due to radiative heating and a weakening of the negative tendencies due to latent heating. In particular, positive tendencies due to radiative heating at 370 K are weakest within the anticyclonic vortices and strongest toward the convective core of the monsoon. Although the net effect of both terms is to weaken the vortices, the total positive tendencies are weakest from the center toward the southeast for IP-mode vortices and from the center toward the southwest for TP-mode vortices (with a second local minimum in the far southeast). The distribution associated with BH-mode vortices has a more complex structure, with minima to the north and southeast, relatively strong positive tendencies near the vortex center, and stronger positive tendencies to the east and west.

On average, diabatic heating exerts a ~~direct influence on the southward movement of PV tendency. This is illustrated in Fig. 6, which indicates that~~ southward pull on anticyclonic vortices at 370 K, with both latent heating and ~~background radiation contribute to a small or negative PV tendencyto the south of the anticyclone. But~~ radiative processes contributing to this tendency. However, the magnitude of ~~diabatic heating is even smaller than the~~ the diabatic heating term is small relative to

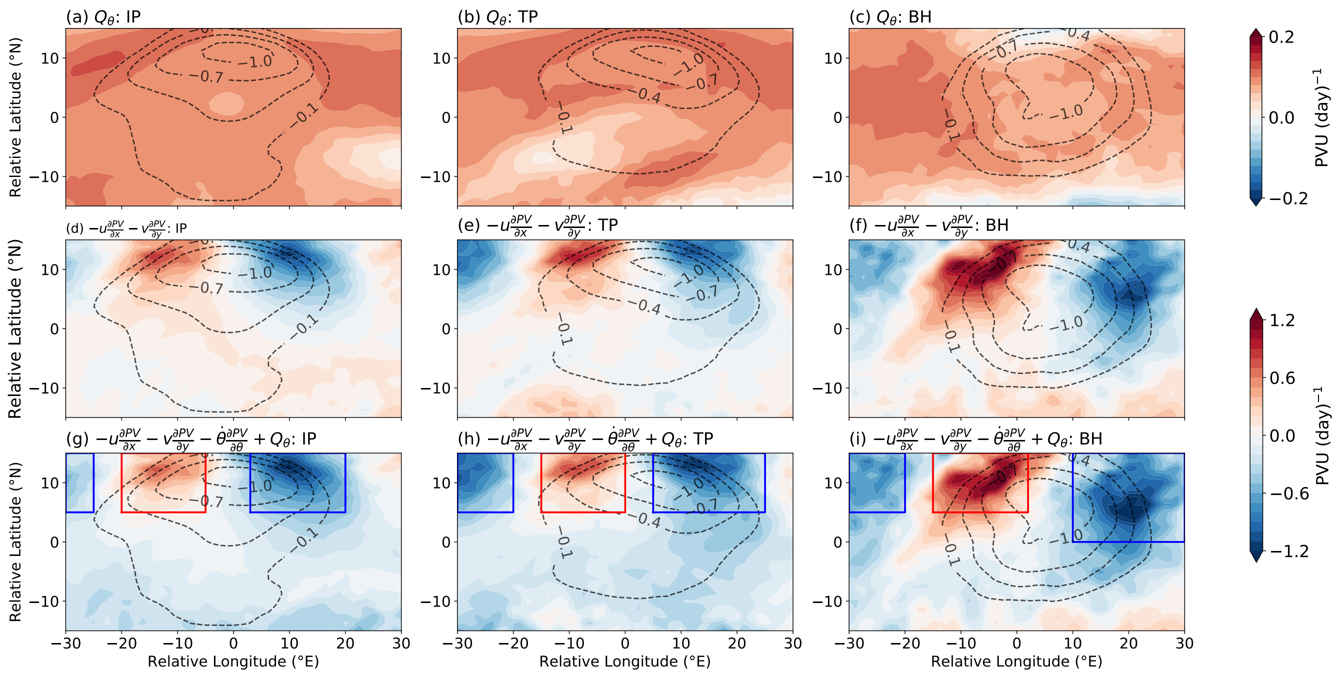

Figure 12. PV tendencies from (a)-(c) the vertical divergence of diabatic heating, (d)-(f) horizontal advection, and (g)-(i) their sum along with vertical advection on the 370 K isentropic surface. Black dashed contours show the PV anomaly at 370 K from −1 to 0 PVU at an interval of 0.3 PVU. The horizontal and vertical axes indicate longitude and latitude relative to the vortex center, respectively. The red boxes in the lower row indicate the main areas of net positive PV tendencies, while the blue boxes indicate regions of net negative PV tendencies.

that of horizontal advection, the vertical advection acts to enhance the PV tendency to the south of the anticyclone, resulting in significant upward motion on the southern side, see Fig.S2(a)-(c). Collectively, the interactions among particularly north of the vortex center (Fig. 12), the results on ERA5 and MERRA2 are show in Fig. S7 and S8. Vertical advection produces a net negative tendency at 370 K, which is located above the level of zero net radiative heating (Fig. 7a) and therefore represents a supply of low-PV air from lower altitudes. The combined effects of vertical advection, horizontal advection, and total diabatic heating give rise to a tripole pattern produce a tripolar structure associated with the anticyclone (Fig. 12g-i), characterized by convergence to the north and divergence to the northeast and northwest, as shown in Fig. S2(g)-(i). The warm and humid air located to the south and westof negative tendencies to the northeast of the vortex center, positive tendencies to the northwest, and an additional center of negative tendencies further to the west. Warm, moist air with low values of PV is transported upward to the southeast of the vortex and then westward along the southern flank. These two effects combine to produce predominantly negative net tendencies at latitudes south of the vortex center (Fig. 12g-i). Meanwhile, the anticyclone moves northward and upward. As this air cools, latent heat is released at lower levels, resulting in a positive PV tendency in these lower levels.Concurrently, an imbalance in the pressure gradient force at upper levels generates a negative PV tendency, leading to divergence, the anticyclone exhibits atendency to propagate in both the northwest and northeast directions.background zonal flow imports relatively high values of PV from upstream of the vortex and exports relatively low values downstream, explaining the dipole along the northern flank (see also Fig. 6a). This dipole in turn dominates the net PV tendency at latitudes north of the vortex center (Fig. 6d and Fig. 12g-i).

The PV tendency equation provides a useful ~~tool on how the intensification and locations of ASMA change within 6 hours interval~~framework for examining how vortices within the ASMA evolve over time. To better quantify the ~~intensification and~~ contributions of each term ~~,~~ to intensification and propagation, we take the minimum PV ~~inside each box (~~tendency inside each of the red and blue ~~box~~ boxes marked in Fig.~~S2 is considered as the value representing the ASMA developmentand is noted as q_{dev}. But the q_{dev} is not directly related to the anticyclone intensification as propagationleads to~~ 12 to represent vortex development. However, this term, which we note as $\dot{q}_{\mathrm{dev}}$, cannot be uniquely related to vortex intensification or propagation: positive or negative PV tendencies ~~aligned to its movement , and intensification makes the anticyclone stronger, so the propagation and intensification are bothaccount for the anticyclone development. The q_{dev} in~~ within each box may result in movement of the vortex center, strengthen or weaken the vortex, or both. To address this, we first decompose $\dot{q}_{\mathrm{dev}}$ into westward and eastward ~~is decomposed as~~

components:

$$\begin{aligned} \dot{q}^{W}_{\mathrm{dev}} &= \dot{q}^{W}_{\mathrm{int}} + \dot{q}^{W}_{\mathrm{prop}} \\ \dot{q}^{E}_{\mathrm{dev}} &= \dot{q}^{E}_{\mathrm{int}} + \dot{q}^{E}_{\mathrm{prop}} \end{aligned} \tag{6}$$

where ~~q_{int} and q_{prop} are the PV tendencies due to anticyclone intensification and propagation. The foundation of this methodology is the tripole pattern of PV tendency. The PV tendency is an indicator of anticyclonic migration, while the tripole pattern indicates a process of intensification. The q_{int} can be defined as~~ $\dot{q}_{\mathrm{int}}$ represents PV tendencies that change the strength of the vortex and $\dot{q}_{\mathrm{prop}}$ represents PV tendencies resulting in propagation.

$$\begin{aligned} q^{W}_{int} &= \left[q^{W}_{int}\right] + \left[q^{center}_{int}\right] \\ q^{E}_{int} &= \left[q^{E}_{int}\right] + \left[q^{center}_{int}\right] \end{aligned}$$

~~where $\left[q^{W}_{int}\right]$ and $\left[q^{E}_{int}\right]$ is the PV tendency averaged within the box centered at westside and eastside (negative PV tendency, the blue box), respectively, $\left[q^{center}_{int}\right]$ is the averaged PV tendency inside the red box for positive PV tendency. The geographical ranges of the western blue box, the eastern blue box, and the red box in three modes are shown in Table 3.~~

~~To simplify the interpretation of the vertical advection terms, the PV tendency is converted from the pressure level coordinate to 370 K isentropic surface, as shown in Fig. 7. Since air parcels generally flow along isentropic surfaces (in the absence of diabatic heating), the advection is a much more accurate representation of how PV is actually being transported by the wind. The diabatic term Q is often the most crucial for understanding the intensification of anticyclone. By analyzing the PV tendency on 370 K, you can directly isolate and quantify the impact of latent heat release (from convection) or radiative cooling on the PV structure in three modes. The strong convective heating beneath the 370 K surface will create a strong positive PV tendency on that surface, directly linking vapor processes to large-scale dynamics. The diabatic heating term (Q) generates negative PV~~

Table 3. The relative geographysical ranges (relative longitude and latitude), the eastward direction is defined as positive, while also the northward direction is taken as negative positive in the tripole patterns of three modes.

Mode	Western box (blue)	Center box(red)	Eastern box (blue)
IP	5°to 15°; -30°to -25°	5°to 15°; -20°to -5°	5°to 15°; -3°to 20°
TP	5°to 15°; -30°to -20°	5°to 15°; -15°to 0°	5°to 15°; 5°to 25°
BH	5°to 15°; -30°to -20°	5°to 15°; -15°to 2°	0°to 15°; 10°to 30°

tendencies south of the anticyclone centers, e.g. consistent with strong latent heating from deep monsoon convection in BH, as shown in Fig. 7. The negative PV tendency strengthens the anticyclonic circulation, the horizontal PV advection (middle row) introduces a tripole patterns.

The PV tendency from (a1)-(a3) zonal advection ($-u\partial q/\partial x$), (b1)-(b3) meridional advection ($-v\partial q/\partial y$), (c1)-(c3) vertical advection ($-\omega\partial q/\partial p$), (d1)-(d3) PV tendency ($\partial q/\partial t$), (e1)-(e3) latent heating (Q_{LH}), and (f1)-(f3) total diabatic heating (Q). The PV anomaly is contoured in black dashed line with -0.1 PVU interval from -0.1 to -0.5 PVU and potential temperature is plotted in gray line. The longitudinal extent of anticyclone is denoted by relative longitude. The first, second, and third column is the calculation from JRA-3Q, ERA5, and MERRA-2 respectively. This methodology is designed to unravel the tripolar pattern of PV tendencies to the north of the vortex center, where PV anomalies are largest (Fig. 12). Accordingly, we define the intensification term $\dot{q}_{\text{int}}$ as

$$\begin{aligned} \dot{q}^{W}_{\text{int}} &= \left[\dot{q}^{\blacktriangleleft}_{\text{int}}\right] + \left[\dot{q}^{\triangle}_{\text{int}}\right] \\ \dot{q}^{E}_{\text{int}} &= \left[\dot{q}^{\triangle}_{\text{int}}\right] + \left[\dot{q}^{\blacktriangleright}_{\text{int}}\right] \end{aligned} \qquad (7)$$

where $[\dot{q}^{\blacktriangleleft}_{\text{int}}]$ and $[\dot{q}^{\blacktriangleright}_{\text{int}}]$ are the minimum (most negative) PV tendencies within the blue boxes to the west and east of the vortex center, respectively, and $\left[\dot{q}^{\triangle}_{\text{int}}\right]$ is the minimum PV tendency within the red box. The geographical ranges of the three boxes for each mode are listed in Table 3.

The PV tendency from (a)-(c) background radiation Q_{rad}, (d)-(f) latent heating Q_{LH}, and (g)-(i) total diabatic heating Q in IP, TP, and BH regions (from left to right) on 200 hPa. The black dashed contours show the PV anomaly at 100 hPa which contours from -1 to 0 PVU with interval of 0.3 PVU. The longitudinal and latitudinal extents are the main area of anticyclone. All analyzed patterns feature dashed contours (representing anticyclonic circulation) and shaded regions indicating PV tendency (units: PVU day^{-1}), with axes defined by relative longitude (°E) and latitude (°N) centered on each anticyclone. The diabatic term Q_θ (Eq. (4)) is often crucial for understanding vortex intensification. By analyzing the PV tendency on 370 K, we can directly isolate and quantify the impacts of latent heat release (i.e. convective heating) or radiative heating on the evolution of PV structure in each of the three modes. The rapid decrease in convective heating with height below the 370 K surface creates a negative PV tendency on that surface (Fig. 11), directly linking convective processes to large-scale dynamics. As discussed above, the total diabatic heating term (Q_θ) features local minima consistent with deep convection in the monsoon

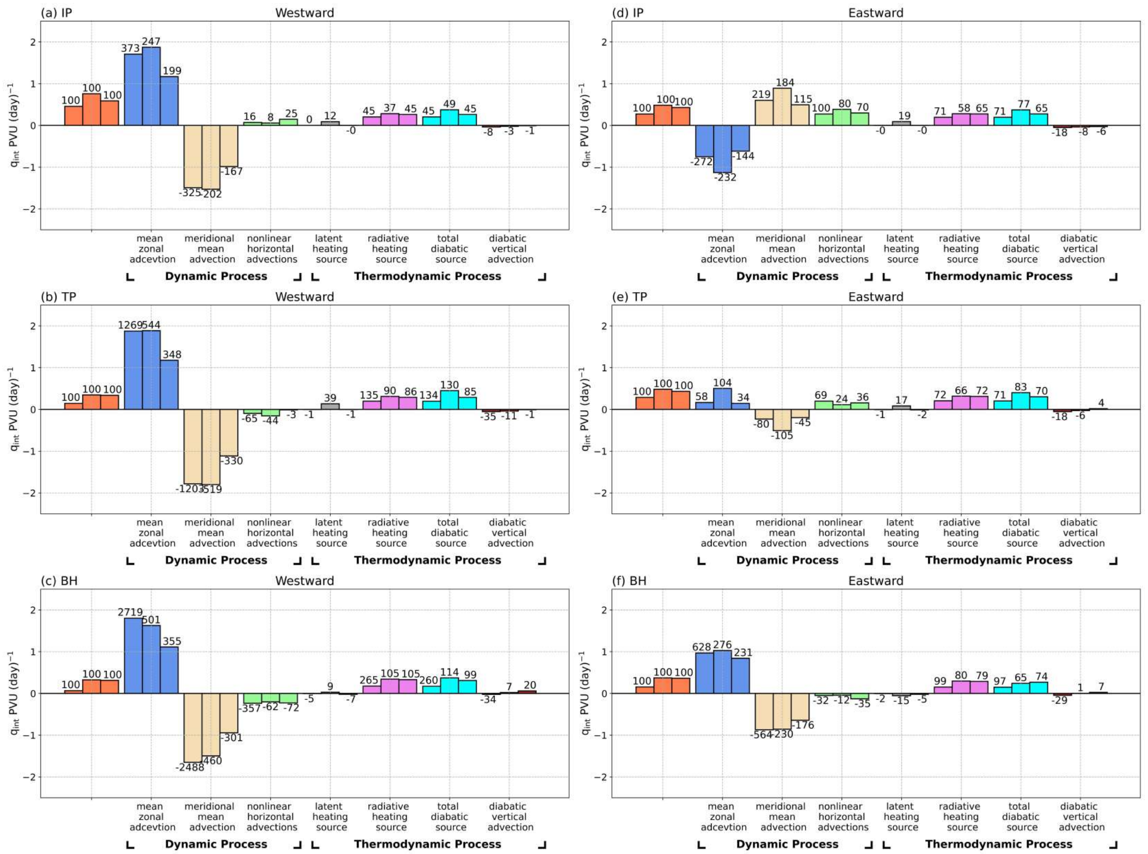

Figure 13. ~~The PV tendency from~~ Contributions of dynamical and thermodynamic processes in Eq. (~~a~~5) ~~-~~to mean PV tendencies to the (~~e~~a–c) ~~vertical advection, (d)-(f) horizontal advection,~~ west of the vortex center and (~~g~~d–f) ~~-(i) sum~~ east of ~~each term from three modes~~ the vortex center on ~~370 k isentropic level. The black dashed contours show~~ the ~~PV anomaly at~~ 370 K ~~which contours from -1~~ isentropic surface. From left to ~~0 PVU with interval~~ right, each group of ~~0.3 PVU. The longitudinal~~ three bars corresponds to JRA-3Q, ERA5, and ~~latitudinal extents are~~ MERRA-2. Numbers on bars denote the ~~main area~~ percentage contribution of ~~anticyclone~~each term. Terms include mean zonal advection, ~~with the red box indicating the main area of divergence~~meridional mean advection, ~~while~~ nonlinear horizontal advection, vertical advection, and the ~~blue boxes signify additional zones of~~ vertical divergence of latent, radiative, and diabatic heating. See section 3.2 for definitions.

core (Fig. 11d-f; Fig. 12a-c). This negative PV tendency reduces radiative spin-down of the anticyclonic circulation, while horizontal PV advection (Fig. 12d-f) introduces the tripole pattern.

~~The contributions of~~ Contributions from each term in Eq. ~~?? to intensification of anticyclone~~ (5) to anticyclone intensification are shown in Fig. ~~8. The~~ 13. A larger positive PV tendency ~~is specifically in relation to the~~ corresponds to a weakening of the anticyclone, ~~otherwise, the~~ whereas negative or smaller PV ~~tendency means the strengthens of anticyclone~~tendencies indicate strengthening. Analysis of PV tendencies ~~reveals that the anticyclone exhibits greater intensification in the eastward compared~~

~~to the westward propagation in IP,but is weaker in TP and BH. The effect~~ suggests that vortex damping is weaker to the east than to the west of IP-mode vortices,while the opposite is true for TP-mode vortices. Little difference is seen for BH-mode vortices. The role of mean zonal advection ~~on the anticyclone differs markedly between these two directions: during westward propagation, mean zonal advection~~ differs substantially between the two directions. Mean zonal advection uniformly acts to weaken the ~~anticyclone, whereas~~ vortex to its west. Zonal advection also acts to weaken the vortex during eastward propagation of TP-mode and BH-mode vortices, but acts to intensify the vortex to the east of IP-mode vortices. In all cases, ~~it strengthens it in IP, but still weakens it in TP and BH. In contrast,~~ the effect of mean meridional advection opposes that of mean zonal advection~~; specifically, mean advection intensifies cyclones in the west while diminishing anticyclones in the east. However, these~~ . These opposing effects largely ~~cancel out each other~~ compensate each other (see also Fig. 6c), although one term ~~tends to predominate when their combined effect is considered~~may slightly exceed the other depending on the specific dynamical regime. The contribution of ~~the~~ nonlinear horizontal advection ~~term is very smallcomparing to the horizontal advection. Given that the anticyclone is situated at an altitude corresponding to the 200 hPa to 100 hPa pressure levels, the~~ is comparatively small, but typically acts to weaken IP-mode vortices and strengthen BH-mode vortices in both directions, and compensate between east and west for TP-mode vortices.

As the 370 K isentropic surface is located near the tropopause, water vapor content is ~~substantially low, thereby rendering the effect and vertical gradient of latent heat release comparatively insignificant relative to the total diabatic heating.Within the non-adiabatic heating components, longwave and shortwave radiation referred to as background radiation in Fig. S2 predominate, leading to~~ relatively low. Moreover, deep convection reaching this level is rare to the north of the ~~attenuation of the ASMA.The q_{dev}, q_{int}, and q_{prop} from reanalysis data~~ vortex centers, where the analysis summarized in Fig. 13 is focused. Among the diabatic components, the vertical divergence of radiative heating dominates in these regions. This term acts to weaken the vortex (see also Fig. 11a-c).

The components $\dot{q}_{\mathrm{dev}}$, $\dot{q}_{\mathrm{int}}$, and $\dot{q}_{\mathrm{prop}}$ derived from the three reanalysis products are shown in Fig.~~9, the eastward development , propagation of ASMA is stronger than in eastward in~~ 14, where $\dot{q}_{\mathrm{prop}}$ is defined as $\dot{q}_{\mathrm{dev}} - \dot{q}_{\mathrm{int}}$. The eastward development and propagation terms are stronger than those associated with westward development in the TP and BH modes. ~~Both the intensification and propagation are negative PV tendency, but the intensification is positive~~ By contrast, the net intensification term remains positive (i.e. damping vortex intendity) due to the presence of the positive PV tendency ~~pole in the~~ center as illustrated in Fig.~~S2 and Fig. 7.~~ 12.

~~The values representing the PV tendency on 370 K for (a-c) westward and (d-f) eastward, the intensification of anticyclone, as attributed to various terms, are depicted in terms of their relative contributions (%). The bars for each term, organized in groups of three reanalysis products (JRA-3Q, ERA5, MERRA-2) from left to right. The numbers on the bar chart represent the percentages (%) of component contributions~~

~~The q_{dev}, q_{int}, and q_{prop} from reanalysis. The values denoted to each bar refer to the relative contribution (%) and PV tendency. The westward and eastward of anticyclone propagation and intensification is represented by the diagonal and dot texture, respectively.~~

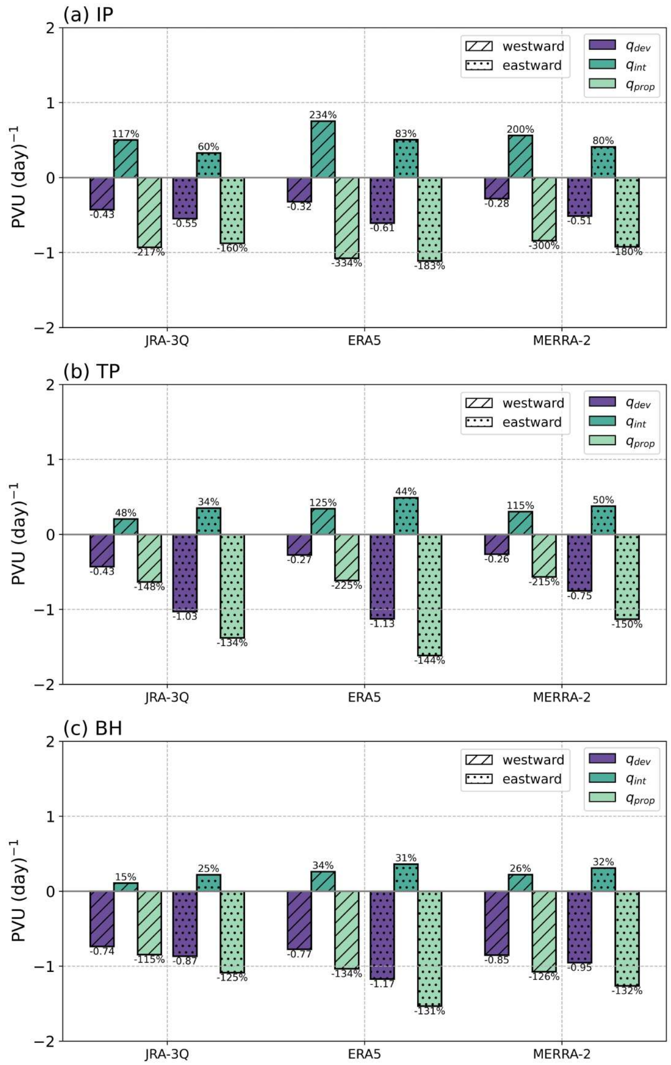

Figure 14. Relative contributions (%) of dynamical and thermodynamic processes to the PV tendency at 370 K during anticyclone intensification for (a–c) westward propagation and (d–f) eastward propagation. Each group of three bars corresponds to JRA-3Q, ERA5, and MERRA-2 (left to right). Numbers on bars denote the percentage contribution of each term. Terms include mean zonal advection, mean meridional advection, nonlinear horizontal advection, vertical advection, and total diabatic heating.

5 Discussion

Our findings on the ~~ASMA's~~ trimodal structure, PV tendency dynamics, and ~~eddy-shedding behavior build directly on foundational work by~~ eddy shedding behavior of the ASMA build upon the work of Siu and Bowman (2020), while ~~resolving~~ helping to resolve key discrepancies and quantifying previously unaddressed mechanisms. A central debate in ASMA research ~~revolves~~

~~around its modality, proposed a dominant bimodal structure(~~concerns its modal structure. Early studies centered around the concept of bimodality in the ASMA, due in large part to the strong preference toward the IP and TP ~~of South Asian High)~~ ~~based on~~ modes in the NCEP-NCAR reanalysis with support from climate model simulations (Zhang et al., 2002; Zhou et al., 2006; Yan et al., 2011). Nützel et al. (2016) challenged this bimodality based on analysis of 100 hPa geopotential height from ~~former reanalysis products (JRA-25, ERA-I~~the previous generation of reanalysis products used in this work (i.e. ERA-Interim, JRA-55, and MERRA~~, etc.~~), finding clear bimodality only in the NCEP-NCAR and NCEP-DOE reanalyses. They proposed that, rather than being bimodal, the center of the ASMA fluctuates across the longitudinal span between the IP and TP centers, neglecting the Western Pacific/BH mode. ~~In contrast, our analysisuses three modern ,~~ Our analysis, which employs three modern high-resolution reanalysis datasets (ERA5, JRA-3Q, and MERRA-2) and tracks vortices on the 370 K isentropic surface~~to track the vortex. We discover the BH (135°–150°E) as a third mode, this consistency across datasets aligns with~~ , supports the modality of the ASMA and highlights the BH within 135°E–150°E as a robust third mode. The consistency across the three reanalysis products supports the findings of Siu and Bowman (2020), who ~~first documented BH's frequent occurrence using MSF~~documented the frequent occurrence of BH vortices using MSF based on the ERA-Interim reanalysis. The discrepancy with Nützel et al. (2016) ~~stems from their reliance on coarser~~ may arise from two factors. First, Nützel et al. (2016) used pressure-level data (100~~hPa)~~ hPa) on a slightly higher level and coarser spatial grid, where BH signals ~~are masked by zonal flow, whereas our isentropic analysis isolates~~ may be obscured by strong zonal flow. The isentropic framework adopted here better resolves the UTLS region~~where weak~~ , where weaker anticyclonic centers are ~~most distinct.~~ more clearly resolved. Second, Nützel et al. (2016) focused on the June–August period of the peak South Asian monsoon. Our results indicate that the BH mode emerges mainly during August–September, as the Western North Pacific maritime component of the monsoon matures (Wu and Wang, 2001; LinHo and Wang, 2002).

The PV tendency ~~diagnostic in this study advances the work pioneered by~~ diagnostics presented here extend the work of Garny and Randel (2013), who ~~linked~~ associated low-PV regions ~~to~~ with convective heating but did not explicitly quantify the processes ~~driving PV temporal changes~~governing PV temporal evolution. Garny and Randel (2013) ~~noted that preexisting~~ also noted that pre-existing low-PV conditions over the Asian monsoon ~~domain complicates separating~~ region complicate the separation of intrinsic ASMA intensification from background variability~~, a challenge we address~~ . This issue is addressed in the present study by decomposing PV tendency into dynamical (horizontal ~~/~~and vertical advection) and thermodynamic (latent heating ~~,~~ and radiation) components. Our results ~~show~~ indicate that mean zonal and meridional advection ~~are the primary drivers of PV tendency, with diabatic heating as a critical~~ dominate the PV tendency. However, these tendencies largely offset each other, allowing diabatic heating to act as an important modulator (Fig. 8a). Manney et al. (2021) documented the ASMA ~~'s core on 350–410~~ core on 350–410 K isentropic surfaces, but did not ~~explore PV dynamics, our work fills this gap by demonstrating how tripole PV tendency patterns (positive at the center, negative eastward/westward) drive the anticyclone's eastward and westward propagation~~ investigate PV dynamics. Here, we demonstrate that a tripolar PV tendency structure (positive near the centre and negative to the east and west) governs the zonal propagation of the anticyclone across its three modes.

~~Eddy shedding is an important driver of ASMA intraseasonal variability, it further highlights the interplay between our findings and prior studies. first identified westward eddy shedding of ASMA, attributing it to baroclinic instability, while~~

linked eastward shedding to BH formation without quantifying underlying mechanisms. Our PV tendency analysis clarifies these processes, westward-shedding eddies (primarily from the IP mode) are driven by mean zonal advection (positive PV tendencies that weaken the anticyclone) and background radiation (damping effects), explaining their transient nature (Table S1). In contrast, eastward shedding (from the TP mode) is sustained by latent heating over the Western Pacific, which generates strong negative PV tendencies (enhancing anticyclonic vorticity) that convert shed eddies into persistent BH centers (Fig. 10 and 11). This directional dependence aligns with 's focus on PV transport but extends it by showing how horizontal advection and diabatic heating collaborate to shape shedding behavior with eastward shedding vortices strengthened by mean zonal advection in the IP mode and latent heating in the BH mode.

Regional characteristics (continental vs. marine) Regional characteristics, particularly those related to the underlying surface, further modulate ASMA dynamics, as . These effects are reflected in the distinct drivers of each mode. The IP mode is shaped by continental-scale wind advection and moderate diabatic forcing; , the TP mode is distinguished by plateau-enhanced latent heating strong latent heating along the southern slope of the Himalayas and the elevated heating of the Tibetan Plateau (Fig. 6e), which amplifies PV tendency anomalies (Fig. 10 and 11); , and the BH mode is governed by strong convective diabatic heating diabatic heating that emerges over the Western Pacific and marine dynamical-advective interactions. Future during the later part of the monsoon heating. These observations are consistent with the interpretation of Randel and Park (2006), who argued that distinct modes of the ASMA are aligned with the warmest tropospheric columns. In this context, future work should explore how teleconnections(e.g. ENSO;) modulate these modal interactions and eddy-shedding frequencies (e.g. ENSO; Yan et al., 2018) modulate ASMA modality and eddy shedding frequency, as well as the impact of anthropogenic forcing on ASMA's (Tweedy et al., 2021; Qie et al., 2025) on the stability and variability directions that build on 's work for a more comprehensive understanding of UTLS circulation driversof the ASMA.

The PV tendency anomalies from (a)-(c) background radiation Q_{rad}, (d)-(f) latent heating Q_{LH}, and (g)-(i) total diabatic heating Q in IP, TP, and BH regions (from left to right) on 200 hPa. The black dashed contours show the PV anomaly at 100 hPa which contours from -1 to 0 PVU with interval of 0.3 PVU.

The PV tendency anomalies from (a)-(c) vertical advection, (d)-(f) horizontal advection, and (g)-(i) sum of each term from three modes on 200 hPa. The black dashed contours show the PV anomaly at 100 hPa which contours from -1 to 0 PVU with interval of 0.3 PVU.

6 Conclusions

This study systematically clarifies the key dynamical mechanisms of the ASMA through comprehensive analyses of three state-of-the-art reanalysis datasets and via a PV tendency diagnostic, thereby contributing to resolving ASMA's intensification, development, propagation, and temporal evolution. A . One definitive finding is the trimodal structure of the ASMA during boreal summer, which is characterized by persistent anticyclonic centers over the IP, TP, and BH with a distinct seasonality. This finding complements the bimodality perspective clarifies the challenge to bimodality reported by Nützel et al. (2016). By leveraging the 370 K isentropic surface identified as the climatological core of the ASMA and a , suggesting that the broader distributions of ASMA center in more recent reanalyses results from seasonal migration of the primary modes in longitude. Our multi-center vortex tracking algorithm , this study discovers further affirms that the BH constitutes a persistent mode rather than transient atmospheric noise. This trimodal signature is is a distinct mode that emerges late in the monsoon season as the Western North Pacific monsoon matures (LinHo and Wang, 2002; Siu and Bowman, 2020). The trimodality and its dominant seasonality are consistent across the three datasetsrecent reanalysis products, with only minor discrepancies observed in MERRA-2, which may be attributed to differences in data assimilation schemes and vertical resolution among . The drivers of vortex evolution highlighted by the composite PV tendency analysis are less robust across the reanalyses, emphasizing continued uncertainties in mechanistic attribution using reanalysis products. New budget diagnostics that explicitly include tendencies due to data assimilation (Wright et al., 2025; Zhang et al., 2025) may help to disentangle these uncertainties.

The ASMA-specific PV tendency diagnostic developed herein extends the PV-based analytical method pioneered by Garny and Randel (2013) by quantitatively disentangling the dynamical and thermodynamical drivers of ASMA evolution. Results demonstrate that mean zonal and meridional advection work as are the predominant drivers of PV tendency, while total diabatic heating (encompassing latent heating and background radiation) exerts a critical modulating effect. This diagnostic effectively captures a characteristic tripole PV tendency pattern with positive anomalies at the anticyclonic core and negative anomalies to the east and west which enables the decoupling of ASMA intensification from zonal propagation, addressing a notable limitation of conventional PV analysis approaches. Specifically, latent heating enhances the BH mode via negative PV tendencies, whereas background radiation induces weakening effects on the ASMA as a whole, highlighting the mode-specific regulatory role of thermodynamic processes.

Furthermore, eddy shedding dynamics exhibit Eddy shedding is an important driver of ASMA intraseasonal variability with intrinsic links to the ASMA's trimodal structure , with distinct directional drivers governing the persistence of each mode. Eastward eddy shedding from the TP mode, sustained by intense latent heating associated with deep convection over the western Pacific, facilitates the conversion of transient eddies into persistent BH centers. In contrast, westward eddy shedding from the IP mode is primarily driven by mean zonal advection and background radiation. These directional differences are inherently tied to regional underlying surface characteristics: the IP and TP modes are dominated by continental scale dynamical processesand moderate diabatic forcing, while the BH mode is shaped by marine influenced convective heating. Collectivelytrimodal structure of the ASMA. Popovic and Plumb (2001) first identified westward eddy shedding of ASMA, attributing it to baroclinic instability, while Siu and Bowman (2020) linked eastward shedding to BH formation without quantifying underlying mechanisms. Recent observational and modeling studies have reaffirmed the importance of eddy shedding dynamics for the evolution of UTLS composition (e.g. Pan et al., 2022; Bak et al., 2025). Our PV tendency analysis could help to clarify these processes, these including key differences between the dynamics of westward-shedding eddies and eastward-shedding eddies. Such an analysis will require a robust, objective approach to identifying eddy shedding events, which will be a central goal of follow-up work.

Collectively, our findings establish a unified theoretical framework for understanding ASMA variability, underscoring the intricate interplay between dynamical advection, thermodynamic forcing, and modal structure. This work not only advances the scientific understanding of UTLS circulation dynamics ~~but also provides~~ while also providing a robust physical basis for improving the predictability of monsoon-related regional climate variability and UTLS tracer transport.

Author contributions. Ninghui Li contributed to conceptualization, data analysis, and drafting the original manuscript; Jonathon Wright provided supervision, draft editing, participated in data analysis, and curated the data; Philip Rupp Alison Ming and Shenglong Zhang were involved in data analysis and manuscript review/editing; Jie Gao contributed to result analysis, provided supervision on the research, and participated in manuscript review/editing.

Code and data availability. ERA5 products (Hersbach et al., 2017, 2023) were acquired from the Copernicus Climate Data Store (CDS; https://cds.climate.copernicus.eu). JRA-3Q reanalysis products (JMA, 2022, 2023) were acquired from the Data Integration and Analysis System (DIAS; https://search.diasjp.net/en/dataset/JRA3Q) archive maintained by the Japan Agency for Marine-Earth Science and Technology (JAMSTEC) and the University of Tokyo and from the National Center for Atmospheric Research (NCAR) Geoscience Data Exchange (https://gdex.ucar.edu/datasets/d640000). MERRA-2 (GMAO, 2015a, b) products were acquired from the NASA Goddard Earth Sciences Data and Information Services Center (GES DISC; https://disc.gsfc.nasa.gov). Python scripts used to produce the analyses and figures in this study are available on request from the authors.

Competing interests. One of the authors is a guest coordinator for the "SPARC Reanalysis Intercomparison Project (S-RIP) Phase 2" special issue in Weather and Climate Dynamics. The authors have no other competing interests to declare.

Acknowledgements. We would like to thank Dr. Leong Wai Siu and Xiangliang Zhang for the advice in vortex tracking. And the paper is benifited a lot from the discussion with Dr. Shenglong Zhang and YuanRui Chen. This research is supported by the Department of Science and Technology of Shandong Province (ZR2024QD136), and the National Science Foundation of China (grant number 42275053).

References

Amemiya, A.: Dynamics of the quasi-biweekly variability of the Asian monsoon anticyclone, Ph.D. thesis, The University of Tokyo, 2018.

Amemiya, A. and Sato, K.: A Two-Dimensional Dynamical Model for the Subseasonal Variability of the Asian Monsoon Anticyclone, Journal of the atmospheric sciences, 75, 3597–3612, https://doi.org/10.1175/JAS-D-17-0208.1, 2018.

Andrew, D. G., Holton, J. R., and Leovy, C. B.: Middle atmosphere dynamics, Academic Press Inc.,Orlando, FL, https://www.osti.gov/biblio/5936274, 1986.

Bak, J., Kim, J., Koo, J.-H., Pan, L. L., Ryoo, J.-M., Newman, P. A., Franchin, A., Liu, X., Abad, G. G., Lee, H.-J., Jeon, W., and Kim, C.-H.: An Integrated Analysis of Ozone and Carbon Monoxide Over the Western Pacific Using Satellite and Aircraft Measurements During the ACCLIP Summer Campaign 2022, J. Geophys. Res. Atmos., 130, https://doi.org/10.1029/2024jd042771, 2025.

Bian, J., Li, D., Bai, Z., Li, Q., Lyu, D., and Zhou, X.: Transport of Asian surface pollutants to the global stratosphere from the Tibetan Plateau region during the Asian summer monsoon, Natl. Sci. Rev., 7, 516–533, https://doi.org/10.1093/nsr/nwaa005, 2020.

Charney, J. G.: On the scale of atmospheric motions, Geofysiske Publikasjoner, 17, 1–17, 1948.

Enomoto, T.: Interannual Variability of the Bonin High Associated with the Propagation of Rossby Waves along the Asian Jet, Journal of the Meteorological Society of Japan. Ser. II, 82, 1019–1034, https://doi.org/10.2151/jmsj.2004.1019, 2004.

Enomoto, T., Hoskins, B. J., and Matsuda, Y.: The formation mechanism of the Bonin high in August, Quarterly Journal of the Royal Meteorological Society, 129, 157–178, https://doi.org/https://doi.org/10.1256/qj.01.211, 2003.

Ertel, H.: Ein neuer hydrodynamischer Wirbelsatz, Meteorologische Zeitschrift, 59, 271–281, 1942.

Fairlie, T. D., Vernier, J. P., Natarajan, M., and Bedka, K. M.: Dispersion of the Nabro volcanic plume and its relation to the Asian summer monsoon, Atmospheric Chemistry and Physics, 14, 7045–7057, https://doi.org/10.5194/acp-14-7045-2014, 2014.

Fu, R., Hu, Y., Wright, J. S., Jiang, J. H., Dickinson, R. E., Chen, M., Filipiak, M., Read, W. G., Waters, J. W., and Wu, D. L.: Short circuit of water vapor and polluted air to the global stratosphere by convective transport over the Tibetan Plateau, Proc. Nat. Acad. Sci. USA, 103, 5664–5669, https://doi.org/10.1073/pnas.0601584103, 2006.

Fujiwara, M., Wright, J. S., Manney, G. L., Gray, L. J., Anstey, J., Birner, T., Davis, S., Gerber, E. P., Harvey, V. L., Hegglin, M. I., Homeyer, C. R., Knox, J. A., Krüger, K., Lambert, A., Long, C. S., Martineau, P., Molod, A., Monge-Sanz, B. M., Santee, M. L., Tegtmeier, S., Chabrillat, S., Tan, D. G. H., Jackson, D. R., Polavarapu, S., Compo, G. P., Dragani, R., Ebisuzaki, W., Harada, Y., Kobayashi, C., McCarty, W., Onogi, K., Pawson, S., Simmons, A., Wargan, K., Whitaker, J. S., and Zou, C.-Z.: Introduction to the SPARC Reanalysis Intercomparison Project (S-RIP) and overview of the reanalysis systems, Atmos. Chem. Phys., 17, 1417–1452, https://doi.org/10.5194/acp-17-1417-2017, 2017.

Garny, H. and Randel, W. J.: Dynamic variability of the Asian monsoon anticyclone observed in potential vorticity and correlations with tracer distributions, Journal of Geophysical Research: Atmospheres, 118, 13,421–13,433, https://doi.org/10.1002/2013JD020908, 2013.

Gelaro, R., McCarty, W., Suárez, M. J., Todling, R., Molod, A., Takacs, L., Randles, C. A., Darmenov, A., Bosilovich, M. G., Reichle, R., Wargan, K., Coy, L., Cullather, R., Draper, C., Akella, S., Buchard, V., Conaty, A., Silva, A. M. D., Gu, W., Kim, G.-K., Koster, R., Lucchesi, R., Merkova, D., Nielsen, J. E., Partyka, G., Pawson, S., Putman, W., Rienecker, M., Schubert, S. D., Sienkiewicz, M., and Zhao, B.: The Modern-Era Retrospective Analysis for Research and Applications, Version 2 (MERRA-2), Journal of Climate, 30, 5419–5454, https://doi.org/10.1175/JCLI-D-16-0758.1, 2017.

GMAO: MERRA-2 inst3_3d_asm_Nv: 3d,3-Hourly,Instantaneous,Model-Level,Assimilation,Assimilated Meteorological Fields V5.12.4, https://doi.org/10.5067/WWQSXQ8IVFW8, last Accessed: February 2024, 2015a.

GMAO: MERRA-2 tavg3_3d_tdt_Np: 3d,3-Hourly,Time-Averaged,Pressure-Level,Assimilation,Temperature Tendencies V5.12.4, https://doi.org/10.5067/9NCR9DDDOPFI, last Accessed: February 2024, 2015b.

Hersbach, H., Bell, B., Berrisford, P., Hirahara, S., Horányi, A., Muñoz-Sabater, J., Nicolas, J., Peubey, C., Radu, R., Schepers, D., Simmons, A., Soci, C., Abdalla, S., Abellan, X., Balsamo, G., Bechtold, P., Biavati, G., Bidlot, J., Bonavita, M., De Chiara, G., Dahlgren, P., Dee, D., Diamantakis, M., Dragani, R., Flemming, J., Forbes, R., Fuentes, M., Geer, A., Haimberger, L., Healy, S., Hogan, R., Hólm, E., Janisková, M., Keeley, S., Laloyaux, P., Lopez, P., Lupu, C., Radnoti, G., de Rosnay, P., Rozum, I., Vamborg, F., Villaume, S., and Thépaut, J.-N.: Complete ERA5 from 1940: Fifth generation of ECMWF atmospheric reanalyses of the global climate, https://doi.org/10.24381/cds.143582cf, last Accessed: February 2024, 2017.

Hersbach, H., Bell, B., Berrisford, P., Hirahara, S., Horányi, A., Muñoz-Sabater, J., Nicolas, J., Peubey, C., Radu, R., Schepers, D., Simmons, A., Soci, C., Abdalla, S., Abellan, X., Balsamo, G., Bechtold, P., Biavati, G., Bidlot, J., Bonavita, M., De Chiara, G., Dahlgren, P., Dee, D., Diamantakis, M., Dragani, R., Flemming, J., Forbes, R., Fuentes, M., Geer, A., Haimberger, L., Healy, S., Hogan, R. J., Hólm, E., Janisková, M., Keeley, S., Laloyaux, P., Lopez, P., Lupu, C., Radnoti, G., de Rosnay, P., Rozum, I., Vamborg, F., Villaume, S., and Thépaut, J.-N.: The ERA5 global reanalysis, Quarterly Journal of the Royal Meteorological Society, 146, 1999–2049, https://doi.org/10.1002/qj.3803, 2020.

Hersbach, H., Bell, B., Berrisford, P., Biavati, G., Horányi, A., Muñoz Sabater, J., Nicolas, J., Peubey, C., Radu, R., Rozum, I., Schepers, D., Simmons, A., Soci, C., Dee, D., and Thépaut, J.-N.: ERA5 hourly data on pressure levels from 1940 to present, https://doi.org/10.24381/cds.bd0915c6, last Accessed: February 2024, 2023.

Honomichl, S. B. and Pan, L. L.: Transport From the Asian Summer Monsoon Anticyclone Over the Western Pacific, Journal of Geophysical Research: Atmospheres, 125, e2019JD032 094, https://doi.org/10.1029/2019JD032094, 2020.

Hoskins, B. J. and Rodwell, M. J.: A Model of the Asian Summer Monsoon. Part I: The Global Scale, Journal of Atmospheric Sciences, 52, 1329 – 1340, https://doi.org/10.1175/1520-0469(1995)052<1329:AMOTAS>2.0.CO;2, 1995.

Hoskins, B. J., McIntyre, M. E., and Robertson, A. W.: On the use and significance of isentropic potential vorticity maps, Quarterly Journal of the Royal Meteorological Society, 111, 877–946, https://doi.org/10.1002/qj.49711147002, 1985.

Hsu, H.-H., Terng, C.-T., and Chen, C.-T.: Evolution of Large-Scale Circulation and Heating during the First Transition of Asian Summer Monsoon, Journal of Climate, 12, 793–810, https://doi.org/10.1175/1520-0442(1999)012<0793:EOLSCA>2.0.CO;2, 1999.

JMA: The Japanese Reanalysis for Three Quarters of a Century, https://doi.org/10.20783/DIAS.645, last Accessed: March 2024, 2022.

JMA: The Japanese Reanalysis for Three Quarters of a Century (JRA-3Q), https://doi.org/10.5065/AVTZ-1H78, 2023.

Kachula, O., Vogel, B., Günther, G., and Müller, R.: An optimization-based approach to track the Asian summer monsoon anticyclone across daily and interannual variability, Atmospheric Chemistry and Physics, 25, 15 171–15 195, https://doi.org/10.5194/acp-25-15171-2025, 2025.

Kosaka, Y., Kobayashi, S., Harada, Y., Kobayashi, C., Naoe, H., Yoshimoto, K., Harada, M., Goto, N., Chiba, J., Miyaoka, K., Sekiguchi, R., Deushi, M., Kamahori, H., Nakaegawa, T., Tanaka, T. Y., Tokuhiro, T., Sato, Y., Matsushita, Y., and Onogi, K.: The JRA-3Q Reanalysis, Journal of the Meteorological Society of Japan. Ser. II, 102, 49–109, https://doi.org/10.2151/jmsj.2024-004, 2024.

LinHo and Wang, B.: The Time–Space Structure of the Asian–Pacific Summer Monsoon: A Fast Annual Cycle View, J. Climate, 15, 2001–2019, https://doi.org/10.1175/1520-0442(2002)015<2001:TTSSOT>2.0.CO;2, 2002.

Lorensen, W. E.: History of the Marching Cubes Algorithm, IEEE Computer Graphics and Applications, 40, 8–15, https://doi.org/10.1109/MCG.2020.2971284, 2020.

Manney, G. L., Santee, M. L., Lawrence, Z. D., Wargan, K., and Schwartz, M. J.: A Moments View of Climatology and Variability of the Asian Summer Monsoon Anticyclone, Journal of Climate, 34, 7821 – 7841, https://doi.org/10.1175/JCLI-D-20-0729.1, 2021.

Martineau, P., Wright, J. S., Zhu, N., and Fujiwara, M.: Zonal-mean data set of global atmospheric reanalyses on pressure levels, Earth System Science Data, 10, 1925–1941, https://doi.org/10.5194/essd-10-1925-2018, 2018.

Nützel, M., Dameris, M., and Garny, H.: Movement, drivers and bimodality of the South Asian High, Atmospheric Chemistry and Physics, 16, 14 755–14 774, https://doi.org/10.5194/acp-16-14755-2016, 2016.

Nützel, M., Brinkop, S., Dameris, M., Garny, H., J Ockel, P., Pan, L. L., and Park, M.: Climatology and variability of air mass transport from the boundary layer to the Asian monsoon anticyclone, Atmospheric Chemistry and Physics, 22, 15 659–15 683, https://doi.org/10.5194/acp-22-15659-2022, 2022.

Pan, L. L., Kinnison, D., Liang, Q., Chin, M., Santee, M. L., Flemming, J., Smith, W. P., Honomichl, S. B., Bresch, J. F., Lait, L. R., Zhu, Y., Tilmes, S., Colarco, P. R., Warner, J., Vuvan, A., Clerbaux, C., Atlas, E. L., Newman, P. A., Thornberry, T., Randel, W. J., and Toon, O. B.: A Multimodel Investigation of Asian Summer Monsoon UTLS Transport Over the Western Pacific, Journal of Geophysical Research: Atmospheres, 127, e2022JD037 511, https://doi.org/10.1029/2022JD037511, 2022.

Ploeger, F., Gottschling, C., Griessbach, S., Groo Ss, J. U., Guenther, G., Konopka, P., M Uller, R., Riese, M., Stroh, F., Tao, M., Ungermann, J., Vogel, B., and von Hobe, M.: A potential vorticity-based determination of the transport barrier in the Asian summer monsoon anticyclone, Atmospheric Chemistry and Physics, 15, 13 145–13 159, https://doi.org/10.5194/acp-15-13145-2015, 2015.

Popovic, J. M. and Plumb, R. A.: Eddy Shedding from the Upper-Tropospheric Asian Monsoon Anticyclone, Journal of the Atmospheric Sciences, 58, 93–104, https://doi.org/10.1175/1520-0469(2001)058<0093:ESFTUT>2.0.CO;2, 2001.

Qian, Y., Zhang, Q., Yao, Y., and Zhang, X.: Seasonal variation and heat preference of the south asia high, Advances in Atmospheric Sciences, 19, 821–836, https://doi.org/10.1007/s00376-002-0047-3, 2002.

Qie, K., Tian, W., Bian, J., Xie, F., and Li, D.: Weakened Asian summer monsoon anticyclone related to increased anthropogenic aerosol emissions in recent decades, npj Climate and Atmospheric Science, 8, 140, https://doi.org/10.1038/s41612-025-01026-8, 2025.

Qie, X., Wu, X., Yuan, T., Bian, J., and Lu, D.: Comprehensive pattern of deep convective systems over the Tibetan Plateau–South Asian monsoon region based on TRMM data, J. Climate, 27, 6612–6626, https://doi.org/10.1175/JCLI-D-14-00076.1, 2014.

Randel, W. J. and Park, M.: Deep convective influence on the Asian summer monsoon anticyclone and associated tracer variability observed with Atmospheric Infrared Sounder (AIRS), Journal of Geophysical Research: Atmospheres, 111, https://doi.org/10.1029/2005JD006490, 2006.

Ren, R., Zhu, C., and Cai, M.: Linking quasi-biweekly variability of the South Asian high to atmospheric heating over Tibetan Plateau in summer, Climate Dynamics, 53, 3419–3429, https://doi.org/10.1007/s00382-019-04713-4, 2019.

Rupp, P. M. and Haynes, P. H.: Spatio-temporal stability analysis applied to monsoon anticyclone flow, Quarterly Journal of the Royal Meteorological Society, 146, 1861–1879, https://doi.org/10.1002/qj.3771, 2020.

Rupp, P. M. and Haynes, P. H.: Zonal scale and temporal variability of the Asian monsoon anticyclone in an idealised numerical model, Weather and Climate Dynamics, 2, 413–431, https://doi.org/10.5194/wcd-2-413-2021, 2021.

Santee, M. L., Manney, G. L., Livesey, N. J., Schwartz, M. J., Neu, J. L., and Read, W. G.: A comprehensive overview of the climatological composition of the Asian summer monsoon anticyclone based on 10 years of Aura Microwave Limb Sounder measurements, Journal of Geophysical Research: Atmospheres, 122, 5491–5514, https://doi.org/10.1002/2016JD026408, 2017.

Siu, L. W. and Bowman, K. P.: Unsteady Vortex Behavior in the Asian Monsoon Anticyclone, Journal of the Atmospheric Sciences, 77, 4067–4088, https://doi.org/10.1175/JAS-D-19-0349.1, 2020.

Tamarin, T. and Kaspi, Y.: The Poleward Motion of Extratropical Cyclones from a Potential Vorticity Tendency Analysis, Journal of the Atmospheric Sciences, 73, 1687–1707, https://doi.org/10.1175/JAS-D-15-0168.1, 2016.

Tegtmeier, S., Krüger, K., Birner, T., Davis, N. A., Davis, S., Fujiwara, M., Homeyer, C. R., Ivanciu, I., Kim, Y.-H., Legras, B., Manney, G. L., Nishimoto, E., Nützel, M., Kedzierski, R. P., Wang, J. S., Wang, T., and Wright, J. S.: Chapter 8: Tropical Tropopause Layer, in: SPARC Report No. 10, WCRP Report 6/2021, edited by Fujiwara, M., Manney, G., Gray, L., and Wright, J. S., pp. 309–389, SPARC, Munich, https://doi.org/10.17874/800DEE57D13, 2022.

Tweedy, O., Oman, L. D., Waugh, D. W., Schoeberl, M. R., Douglass, A. R., and Li, F.: Response of the upper-level monsoon anticyclones and ozone to abrupt CO_2 changes, J. Geophys. Res. Atmos., 126, e2021JD034 903, https://doi.org/10.1029/2021jd034903, 2021.

Vernier, J. P., Fairlie, T. D., Natarajan, M., Wienhold, F. G., Bian, J., Martinsson, B. G., Crumeyrolle, S., Thomason, L. W., and Bedka, K. M.: Increase in upper tropospheric and lower stratospheric aerosol levels and its potential connection with Asian pollution, Journal of Geophysical Research: Atmospheres, 120, 1608–1619, https://doi.org/10.1002/2014JD022372, 2015.

Wang, X., Randel, W., Pan, L., Wu, Y., and Zhang, P.: Transient Behavior of the Asian Summer Monsoon Anticyclone Associated With Eastward Eddy Shedding, Journal of Geophysical Research: Atmospheres, 127, e2021JD036 090, https://doi.org/10.1029/2021JD036090, 2022.

Wei, W., Zhang, R., Wen, M., Rong, X., and Li, T.: Impact of Indian summer monsoon on the South Asian High and its influence on summer rainfall over China, Climate Dynamics, 43, 1257–1269, https://doi.org/10.1007/s00382-013-1938-y, 2014.

Wright, J. S. and Fueglistaler, S.: Large differences in reanalyses of diabatic heating in the tropical upper troposphere and lower stratosphere, Atmos. Chem. Phys., 13, 9565–9576, https://doi.org/10.5194/acp-13-9565-2013, 2013.

Wright, J. S., Sun, X., Konopka, P., Krüger, K., Legras, B., Molod, A. M., Tegtmeier, S., Zhang, G. J., and Zhao, X.: Differences in tropical high clouds among reanalyses: origins and radiative impacts, Atmospheric Chemistry and Physics, 20, 8989–9030, https://doi.org/10.5194/acp-20-8989-2020, 2020.

Wright, J. S., Zhang, S., Chen, J., Davis, S. M., Konopka, P., Lu, M., Yan, X., and Zhang, G. J.: Evaluating reanalysis representations of climatological trace gas distributions in the Asian monsoon tropopause layer, Atmos. Chem. Phys., 25, 9617–9643, https://doi.org/10.5194/acp-25-9617-2025, 2025.

Wu, R. and Wang, B.: Multi-stage onset of the summer monsoon over the western North Pacific, Clim. Dyn., 17, 277–289, https://doi.org/10.1007/s003820000118, 2001.

Xue, X., Chen, W., and Hou, S.: The long-term variation in the South Asia High intensity measured by 150-hPa eddy geopotential height, Meteorology and Atmospheric Physics, 132, 833–844, https://doi.org/10.1007/s00703-020-00723-8, 2020.

Yan, R.-C., Bian, J.-C., and Fan, Q.-J.: The Impact of the South Asia High Bimodality on the Chemical Composition of the Upper Troposphere and Lower Stratosphere, Atmospheric and Oceanic Science Letters, 4, 229–234, https://doi.org/10.1080/16742834.2011.11446934, 2011.

Yan, X., Konopka, P., Ploeger, F., Tao, M., M Uller, R., Santee, M. L., Bian, J., and Riese, M.: El Nino Southern Oscillation influence on the Asian summer monsoon anticyclone, Atmospheric Chemistry and Physics, 18, 8079–8096, https://doi.org/10.5194/acp-18-8079-2018, 2018.

Zarrin, A., Ghaemi, H., Azadi, M., and Farajzadeh, M.: The spatial pattern of summertime subtropical anticyclones over Asia and Africa: A climatological review, International Journal of Climate, 30, 159–173, https://doi.org/10.1002/joc.1879, international Journal of Climatology, 2010.

Zhang, D., Huang, Y., Zhou, B., and Wang, H.: Is There Interdecadal Variation in the South Asian High?, Journal of Climate, 34, 8089–8103, https://doi.org/10.1175/JCLI-D-21-0059.1, 2021.

Zhang, Q., Wu, G., and Qian, Y.: The Bimodality of the 100 hPa South Asia High and its Relationship to the Climate Anomaly over East Asia in Summer, Journal of the Meteorological Society of Japan. Ser. II, 80, 733–744, https://doi.org/10.2151/jmsj.80.733, 2002.

Zhang, S., Chen, J., Wright, J. S., Davis, S. M., Gao, J., Konopka, P., Li, N., Lu, M., Tegtmeier, S., Yan, X., Zhang, G. J., and Zhu, N.: Covariability of dynamics and composition in the Asian monsoon tropopause layer from satellite observations and reanalysis products, Atmos. Chem. Phys., 25, 10 109–10 139, https://doi.org/10.5194/acp-25-10109-2025, 2025.

Zhou, N., Yu, Y., and Qian, Y.: Simulations of the 100-hPa South Asian High and precipitation over East Asia with IPCC coupled GCMs, Advances in Atmospheric Sciences, 23, 375–390, https://doi.org/10.1007/s00376-006-0375-9, 2006.